Phosphoproteomics identifies targets of Mos-MAPK regulating translation and spindle organization in oocyte meiosis

Ivan Avilov[1], Yehor Horokhovskyi[2], Mingfang Cai[1], Aleksander Orzechowski[1], Luisa Welp[3], Henning Urlaub[3], Juliane Liepe[2] and Peter Lenart[1]

[1]Research Group Cytoskeletal Dynamics in Oocytes, [2]Research Group Quantitative and Systems Biology, and [3]Research Group Bioanalytical Mass Spectrometry, Max Planck Institute for Multidisciplinary Sciences, Am Fassberg 11, 37077, Göttingen, Germany

Correspondence to peter.lenart@mpinat.mpg.de

Abstract

The Mos kinase is a constitutive activator of the ERK/MAPK pathway exclusively expressed during oocyte meiosis, mediating key meiotic functions across animal species. While a few of its downstream effectors have been studied in some detail, molecular targets under the control of Mos-MAPK have not yet been identified systematically. Here, we combined live-cell microscopy of starfish oocytes to characterize the cellular phenotypes caused by Mos-MAPK inhibition with phosphoproteomic analysis of synchronous oocyte populations at key transitions. This revealed a large set of proteins involved in regulation of translation through the CPE-element binding protein CPEB to be controlled by Mos-MAPK. Our data indicate that cyclin B is the main target of this regulation to drive the second meiotic division. A second large group of phospho-proteins we found to be controlled by Mos-MAPK are regulators of the actin and microtubule cytoskeleton, in particular regulators of centrosomal microtubule nucleation. Indeed, we show that Mos-MAPK inhibition increases the size of microtubule asters and promotes separation of spindle poles in meiotic anaphase, i.e turning meiotic spindles mitotic-like. Together, here we identified core molecular modules controlled by Mos-MAPK driving key meiotic functions, haploidization and the asymmetric polar body divisions. These molecular modules are highly conserved and are thus likely to be involved in reproductive processes across species including humans. In addition, our work may help understand disease mechanisms when Mos is expressed erroneously, acting as an oncogene.

Introduction

To produce haploid gametes in meiosis, chromosome number needs to be reduced by half, to a single set. Therefore gametes undergo two division cycles, meiosis I (MI) and meiosis II (MII) without DNA replication (S-phase) in between. Skipping the S-phase is mediated by the rapid reactivation of the main mitotic kinase, Cdk1-CyclinB after the first meiotic division, enforcing entry into a second division without intervening interphase. This is manifested at the cellular level by the absence of nuclear reformation between MI and MII. Earlier work in *Xenopus* oocytes showed that reactivation of Cdk1-Cyclin B can be achieved by translation of Cyclin B (Hochegger et al., 2001) and/or dephosphorylation of Cdk1 (Iwabuchi et al., 2000) shortly after completion of MI.

A second specific feature of oocyte meiosis compared to mitotic divisions is that oocyte meiosis is synchronized with fertilization and other events of reproduction by additional cell cycle arrest points (Jessus et al., 2020). Fully grown oocytes universally arrest at prophase I that is released by the maturation hormone. This is followed by a second arrest called 'CSF arrest' (cytostatic factor arrest) that synchronizes meiotic progression of the oocyte with fertilization.

Finally, a third key feature of oocyte meiosis is to restrict the number of fertilization-competent gametes to only one, in order to preserve all nutrients for a single large egg cell to support embryo development. This necessitates that the other daughter cells produced by female meiosis are unviable to avoid gamete competition. This is achieved by an extremely asymmetric division of the oocyte, producing tiny, non-viable polar bodies and a single egg cell (Severson et al., 2016).

Each of these specialized features of oocyte meiosis are essential for producing a haploid, fertilizable egg. Strikingly, after fertilization in the same egg cytoplasm mitotic divisions take place with alternating S- and M-phases and without showing any of the meiotic features. What are the molecular mechanisms that mediate the switch between these two distinct forms of division?

The Mos kinase is a constitutive activator of the ERK/MAPK cascade that is expressed and functions specifically and exclusively during oocyte meiosis, and is degraded after fertilization (Dupré et al., 2011). In somatic cells, the ERK pathway is activated by extracellular signals (e.g. growth factors), and is a key pathway controlling proliferation. Therefore, ectopic expression of Mos in somatic cells leads to oncogenic transformation (Oskarsson et al., 1980). However, when Mos is expressed physiologically in oocytes (also referred to as cellular or c-Mos), it plays important roles in meiotic regulation. Mos was first characterized in *Xenopus* oocytes (Sagata et al., 1988), followed by mice (Colledge et al., 1994; Hashimoto et al., 1994), and other deuterostome species including tunicates (Sensui et al., 2012), and starfish (Tachibana et al., 2000). Mos and its conserved functions have since been demonstrated also in the jellyfish *Clytia hemisphaerica* evidencing its ancestral origin (Amiel et al., 2009). However, in protostomes, Mos seems to have secondarily lost its importance as *Drosophila* Mos mutants display normal oocyte development (Ivanovska et al., 2004), and in *C. elegans* the Mos gene is lost (Church et al., 1995).

Mos controls key aspects of the oocyte-specific cell cycle regulation as well as the asymmetric polar body divisions. These functions are mediated by kinases of the MAPK pathway, and primarily by the downstream effector $p90^{RSK}$ (Bhatt and Ferrell, 1999; Mori et al., 2006), with the notable exception of mouse oocytes, in which $p90^{RSK}$ is not involved (Dumont et al., 2005). Firstly, Mos-MAPK is required for meiotic maturation, however this function appears to be restricted to amphibian species (Sagata et al., 1988). Secondly, a more widely conserved function of Mos-MAPK is preventing S-phase between the two meiotic divisions. In *Xenopus*, upon inhibition of Mos-MAPK, oocytes exit MI, reform the nucleus, and initiate S-phase (Sagata et al., 1988). Similarly, in starfish oocytes inhibition of Mos-MAPK abolishes MII, so that MI is followed by the first mitotic cycle (Tachibana et al., 2000). In mouse, studies show somewhat conflicting results, but oocytes certainly show signs of meiotic exit after MI, displaying a reformed nucleus (Araki et al., 1996; Phillips et al., 2002) and an interphase-like chromosome morphology (Verlhac et al., 1996). Thirdly, Mos is required to establish the CSF arrest and thereby synchronize oocyte meiosis with fertilization (Jessus et al., 2020). Indeed, one of the most prominent and most universal effects of

Mos-MAPK inhibition is the loss of CSF arrest leading to parthenogenetic activation of oocytes (Sagata et al., 1988; Colledge et al., 1994; Hashimoto et al., 1994; Tachibana et al., 2000).

Intriguingly, many of the above functions of Mos-MAPK involve increasing or sustaining Cdk1-Cyclin B activity. Studies in *Xenopus* oocytes demonstrated that Mos-MAPK facilitates Cyclin B translation to trigger meiotic maturation, as well as to drive the second meiotic division (Abrieu et al., 2001; Hochegger et al., 2001). For maintenance of the CSF arrest, Mos-MAPK appears to act on Erp1/Emi2 to prevent Cyclin B degradation by the APC/C (Wu and Kornbluth, 2008). However, the detailed molecular mechanisms remain incompletely understood.

Besides meiosis-specific cell cycle regulation, the other main function of Mos-MAPK is to render the meiotic divisions asymmetric. Studies in mice, jellyfish, and other species show that Mos-MAPK inhibition converts the MI and MII spindles to a mitotic-like morphology displaying long, astral-like microtubules (Araki et al., 1996; Verlhac et al., 1996; Bodart et al., 2002; Amiel et al., 2009). The reverse effect has also been observed in tunicates: mitotic embryos ectopically expressing Mos show meiotic-like spindles (Dumollard et al., 2011). Furthermore, in mitosis of somatic cells Mos overexpression leads to meiotic-like spindles positioned off-center and showing less abundant astral microtubules (Fukasawa and Woude, 1995). In mouse oocytes, two spindle regulators controlled by Mos-MAPK, MISS and DOC1R have already been identified and characterized in substantial detail (Lefebvre et al., 2002; Terret et al., 2003). However, a mechanistic model of how Mos-MAPK regulates spindle morphology is still lacking.

Here, we aim to identify the molecular modules under the control of Mos-MAPK by combining phosphoproteomics and live imaging in a uniquely suited model system, the oocytes of the starfish, *Patiria miniata*. As shown in earlier work, Mos-MAPK functions are conserved in starfish: reactivation of Cdk1-Cyclin B at the end of meiosis I, and CSF-like arrest, that in starfish occurs at the G1 phase, are both dependent on Mos-MAPK (Tachibana et al., 2000; Mori et al., 2006). Mos-MAPK has also been shown to control spindle morphology and to affect the asymmetry of division (Ucar et al., 2013). These studies established that U0126, an inhibitor of the downstream MEK1 kinase, effectively and specifically prevents the activation of the Mos-MAPK pathway (Mori et al., 2006; Ucar et al., 2013). They also showed that effects of U0126 closely mirror Mos depletion by anti-Mos morpholino injection (Tachibana et al., 2000), and that of injection of an inhibitory antibody against the downstream effector $p90^{RSK}$ (Mori et al., 2006).

Results

Mos-MAPK drives the second meiotic division

We first imaged live starfish oocytes by high-resolution confocal microscopy to complement the previous detailed biochemical characterization of Mos-MAPK in this species (Tachibana et al., 2000). To this end, we labeled chromatin and microtubules to monitor the effects of U0126 treatment on the two meiotic and subsequent mitotic divisions (Fig 1A). U0126-treated and DMSO-treated control oocytes progressed normally through the initial steps of meiotic maturation: after the addition of the maturation hormone, NEBD commences in 20-25 min. Thereafter, chromosomes congress to the animal pole, indicating that actin- and microtubule-driven mechanisms of chromosome transport are independent of Mos-MAPK (Fig. 1A). The first meiotic spindle then forms and aligns all chromosomes to the metaphase plate both in treated and untreated oocytes (Fig. 1A). The time from NEBD to metaphase I showed no significant difference (Fig. 1B). Overall, these observations are well consistent with biochemical assays that did not detect MAPK activity before metaphase I (Tachibana et al., 2000).

After metaphase I, U0126-treated oocytes showed a strikingly different behavior compared to DMSO-treated controls. Control oocytes, after extrusion of the first polar body, rapidly progress into the second meiotic division and form the metaphase II spindle within ~40 minutes (Fig. 1A). During this transition between the first and second meiotic divisions chromosomes remain condensed and the nuclear envelope does not re-form (Fig. 1A). By contrast, U0126-treated

oocytes exit M-phase after meiosis I evidenced by gradual decondensation of chromatin and reformation of the nucleus, further confirmed by the recruitment of the nuclear envelope marker, lamin B (Fig. 1A, D). These pronuclei that formed in U0126-treated oocytes ~1 hour after metaphase I showed similar morphology to pronuclei in control oocytes that form after the completion of the two meiotic divisions (Fig. 1D). These cellular phenotypes are consistent with previous biochemical assays showing that Mos-MAPK inhibited oocytes enter S-phase after metaphase I (Tachibana et al., 2000).

U0126-treated oocytes did eventually enter a second division, and then began parthenogenetic embryo development without fertilization, consistent with abolished CSF arrest documented earlier (Mori et al., 2006). While by simple counting this may be considered the second meiotic division, by its timing and morphology it clearly corresponds to the first mitosis: it occurs at the time of the first mitotic division in untreated, fertilized oocytes (Fig. 1C), and the spindle is large and features prominent astral microtubules typical to mitotic spindles (Fig. 1A).

To reinforce observations made by live imaging, we performed a morphometric analysis of metaphase spindles stained by immunofluorescence (Fig. 1E-G). In metaphase I, U0126-treated and untreated control spindles have a width and length (excluding centrosomal asters) statistically not different from one another (Fig. 1G). However, when the centrosomal asters are also considered, the diameter of the centrosome increases from ~3.4 μm to almost 5 μm between treated and untreated MI spindles (Fig. 1G). In control oocytes, the metaphase II spindle showed a similar morphology to metaphase I except for an approximately twice-smaller centrosomes, well consistent with the half-reduced centriole number in MII (Borrego-Pinto et al., 2016a). Spindle morphology in the second division in U0126-treated oocytes is strikingly different from normal meiotic metaphase II and in all its measured parameters is indistinguishable from mitotic morphology: spindle length increases from ~9 μm to ~20 μm, and the diameter of the centrosome more than doubles from ~2 μm to ~5 μm between meiotic and mitotic metaphases (Fig 1G).

Taken together, the timing of the divisions, the morphology of pronuclei and metaphase spindles evidence that U0126-treated oocytes proceed directly from meiosis I to parthenogenetic development without undergoing meiosis II. These observations are fully consistent with previous biochemical assays (Tachibana et al., 2000), and demonstrate that Mos-MAPK is required to drive meiosis II and thereby the haploidization of the female gamete.

Phosphoproteomic analysis of Mos-MAPK inhibition at metaphase I

Our data and consistent previous observations thus show that Mos-MAPK drives the second meiotic division. In this process, there is a critical bifurcation point at metaphase I: if Mos activates the MAPK pathway, then the oocyte proceeds to MII without undergoing an S-phase. If the Mos-MAPK pathway is inhibited, the oocytes skip MII entirely and proceed into interphase, S-phase, and a subsequent parthenogenetic development.

Therefore, to identify the downstream targets of Mos-MAPK, we performed a phosphoproteomic analysis of oocytes at this critical transition. Oocytes were isolated from three starfish animals (collected in the wild from natural populations), each treated with U0126 or an equal amount of DMSO (Fig 2A). Synchrony was confirmed by staining a small portion of the sample, which showed 92-96% of metaphase figures. Samples were then processed, enriched for phospho-peptides, and analyzed by multiplexed quantitative tandem mass tag (TMT) mass spectrometry (Fig. 2A).

In total, we quantified 9,035 protein groups, of which 4,716 contained phospho-peptides, 22,822 phospho-peptides in total (Fig. 2B). These numbers were comparable to previously published phosphoproteomic analysis of starfish oocytes (Swartz et al., 2021). Differential expression analysis (DEA) revealed no significant changes in protein levels consistent with previous studies showing that protein levels remain largely constant through meiotic divisions (Swartz et al., 2021). We then used ratios of phosphorylated peptides to their total protein intensities in U0126 *versus* DMSO treated samples (10,880 unique phospho-peptide sequences and 16,535 sequence-

PTM combinations, Fig. 2B). This resulted in 269 unique phospho-peptides that passed the significance threshold of the adjusted p-value of 0.05 (Supplementary File 1). Despite sampling genetically diverse individuals, unsupervised clustering of differentially phosphorylated peptide intensities clearly separated U0126-treated samples from DMSO controls, evidencing an effect much above biological variability (Fig. 2C).

Next, we performed an over-representation analysis to test which biological processes were associated with proteins that underwent differential phosphorylation. This revealed the enrichment of gene ontology (GO) terms related to processes of cell cycle and cytoskeletal regulation (Fig. 2D). Secondly, we used a prediction tool to identify putative human protein kinases responsible for changes in phosphorylation (Johnson et al., 2023). This analysis showed a statistically significant enrichment of kinases related to the Mos-MAPK-pathway: top hits are AGC family of kinases, which include $p90^{RSK}$, the main downstream effector kinase of the Mos-MAPK pathway (Fig. 2E, Supplementary file 3). Expectedly, the STE family, kinases of the MAPK pathway are also identified. We further detected a significant enrichment of the CAMK family, which may be explained by the fact that RSK kinases contain two distinct kinase domains, the second of which belongs to the CAMK family. Additionally, some of the other kinases within the AGC and CAMK families are involved in actin regulation (ROCK, MYLK). Intriguingly, we also observed a significant enrichment of the otherwise unrelated family of Aurora kinases (Fig 2E).

We then manually curated the list of significantly changed phospho-proteins. This confirmed several hits related to cytoskeletal processes and cell cycle regulation consistent with the identified GO-terms. Additionally, we identified a large number of translational regulators, including several of the top hits with the highest enrichment and significance (Fig. 2F). GO-term enrichment did not immediately reveal these hits, since we only identified a specific subset of 11 proteins out of the very large group of 1059 proteins associated with the term "translation". Furthermore, we found changes in the phosphorylation of MAPK pathway components, and identified other proteins involved in DNA replication, repair, chromatin maintenance, transcription, RNA processing, and other processes (Supplemental File 1).

In summary, our phosphoproteomic analysis of U0126-treated oocytes revealed no change in protein levels, and identified a set of 269 unique phospho-peptides, which changed phosphorylation significantly and consistently upon treatment across biological replicates. Automated and manual analyses were in excellent agreement with expectations based cellular phenotypes and biochemical data: translation, cell cycle, and cytoskeletal regulation were the main processes affected, and kinase profiling found the MAPK-pathway and $p90^{RSK}$ to be the major effector kinases.

Phosphoproteomics identifies functional modules regulated by the Mos-MAPK pathway

Next, we used the manually curated hitlist to identify functional modules, i.e. molecular complexes that may mediate cellular processes downstream of Mos-MAPK.

Firstly, we detected dephosphorylation of MEK and the downstream effector $p90^{RSK}$ (Fig. 3), confirming the inhibition of the MAPK pathway (Mori et al., 2006). Secondly, U0126 treatment causes oocytes to exit after meiosis I rather than entering the second meiotic division. Consistently, we detected changes indicating inactivation of Cdk1-Cyclin B. This includes dephosphorylation of the main activator and inhibitor of Cdk1-Cyclin B, the Cdc25 phosphatase, and the Myt1 kinase, respectively (Fig. 3A and B). We also detect dephosphorylation of the APC/C subunit Cdc27 (APC3) responsible for degradation of Cyclin B. Furthermore, Arpp19 and PP2A are also dephosphorylated. PP2A is known to antagonize Cdk1-Cyclin B and has recently been identified as an important regulator of the meiotic cell cycle in starfish oocytes (Swartz et al., 2021). In addition, we detected several changes indicative of an overall signature of M-phase exit, including regulators of DNA replication (Supplemental File 2). Together, the changes are fully consistent with Mos-MAPK inhibition leading to inactivation of Cdk1-Cyclin B, and thus exit from M-phase after MI.

In addition to cell cycle signaling, translational regulation emerged as the most prominent functional module affected by Mos-MAPK inhibition. We identified changes in the phosphorylation status of several components of the cap-dependent translation initiation complex (eIF3A, eIF4B, eIF4G) along with PPM1G, a phosphatase regulator of 4E-BP1 (Liu et al., 2013) (Fig. 3). Among the top hits is LARP1, a translational regulator of mRNAs characterized by a 5' terminal oligopyrimidine (5'TOP) motif typically associated with the mTOR pathway (Berman et al., 2021). LARP1 binds the 5'TOP motif and is thought to play a role in circularizing the transcript by interaction with the PolyA-binding protein (PABP) at the 3' end. Other highest scoring hits are the CPE-element binding protein, CPEB, and the eIF4E transporter, eIF4ENIF1. These proteins form a complex together with Maskin/TACC3 to inhibit translation with eIF4ENIF1 bound to the 5'-cap and CPEB bound to the CPE-element in the 3'UTR (Fig. 3) (Mendez and Richter, 2001; Minshall et al., 2007). Indeed, while no Maskin/TACC3 phospho-peptides passed the significance threshold, we detected many phospho-peptides below significance (Supplemental File 2). Upon phosphorylation, the inhibitory complex dissociates and CPEB recruits the PolyA polymerase PAP to activate translation (Mendez and Richter, 2001). Together, the changes induced by U0126 treatment indicate that Mos-MAPK activates translation in meiosis I by phosphorylation of CPEB and other regulators of CPE-dependent translation.

Another large group of phospho-peptides are regulators of the cytoskeleton, a substantial subset of which are involved in centrosomal microtubule nucleation (Fig. 3). We found components with roles in centrosome maturation, including proteins involved in the recruitment of the pericentriolar material to centrioles (CEP192, CEP44, and POC1), the main pericentriolar material constituent, PCM1, as well as the protein furry (FRY)-like, thought to be important for centrosome integrity early in cell division (Ikeda et al., 2012; Conduit et al., 2015). Secondly, we found several proteins that play a role in nucleating and stabilizing astral microtubules including the general microtubule plus tip binding proteins XMAP215/chTOG and CLIP1 (Slep and Vale, 2007), and GTSE1, a plus tip binding protein that specifically regulates the stability of astral microtubules (Bendre et al., 2016). Furthermore, we identified several members of the kinesin superfamily. A kinesin-4 family member (identified as KIF4/21/27) may be involved in separation of spindle poles in anaphase (Bieling et al., 2010), and the kinesin-3 KIF14 may be required for anaphase in interaction with citron kinase (Gruneberg et al., 2006). Interestingly, a meiosis-specific paralog of KIF14, NabKin was reported to regulate polar body cytokinesis in *Xenopus* oocytes (Samwer et al., 2013).

We also identified several proteins that regulate the actin cytoskeleton (Fig. 3). In particular, regulators of the small GTPases Cdc42, Rac1, and RhoA as well as their downstream effectors have been detected. This includes BCR, which is a GTPase-activating protein for Cdc42, as well as the activator of RhoA, MYO9. We detected a significant dephosphorylation of mDia2 downstream of RhoA, which confirms earlier results demonstrating that mDia2 is a downstream target of Mos-MAPK in starfish (Ucar et al., 2013). Additionally, we found a significant effect on the Cdc42 binding protein MRSK, which recently have been shown to drive the initial, meiosis-specific step of polar body cytokinesis (Bourdais et al., 2023). Finally, we found Rac1 to be dephosphorylated that may be involved in Arp2/3-dependent actin nucleation and act as an antagonist of RhoA during polar body cytokinesis (Halet and Carroll, 2007; Pal et al., 2020).

Taken together, our phosphoproteomic analysis identified highly conserved molecular modules downstream of Mos-MAPK regulating translation and the microtubule as well as the actin cytoskeleton.

Translation of Cyclin B is sufficient to drive the second meiotic division

Our phosphoproteomics thus indicates that Mos-MAPK induces CPE-dependent translation. Studies in *Xenopus* oocytes suggest that timely translation of Cyclin B is a key mechanism to reactivate Cdk1-Cyclin B at the end of MI and thereby drive MII (Hochegger et al., 2001). Thus, we wanted to test the hypothesis that Mos-MAPK may drive MII by driving Cyclin B translation.

To this end, we first blocked Cyclin B translation by injection of an anti-Cyclin B morpholino. Injected oocytes were able to complete the first meiotic division with normal timing and displaying normal spindle morphology (Fig. 4A, B). This is expected as starfish oocytes contain sufficient Cdk1-Cyclin B protein (a.k.a. pre-MPF) to drive MI (Hara et al., 2012). Following MI, however, morpholino-injected oocytes entered interphase, formed nuclei, and stopped further meiotic progression, unlike control oocytes, which entered MII (Fig. 4A). These effects on cell cycle progression are also reflected by the cell-cycle-dependent formation and disassembly of phase-separated condensates of histone H1-Alexa647, which we used here to label chromosomes. These condensates have been shown to form in interphase and dissolve in M-phase (Shakya et al., 2020). Consistently, in control oocytes H1 condensates are observed for only a brief period between the two meiotic divisions, and again at the G1 stage at the end of meiosis (Fig. 4A). By contrast, in Cyclin B morpholino injected oocytes H1 condensates persist after MI, confirming the sustained arrest in interphase (Fig. 4A). Complete inhibition of translation by Emetine caused effects very similar to the Cyclin B morpholino: the formation of the first meiotic spindle with normal morphology followed by re-formation of the nucleus and sustained interphase arrest (Fig. 4C). These data together indicate that translation of Cyclin B alone may be sufficient to drive the second meiotic division.

To test this directly, we injected active Cdk1-Cyclin B complex (Veld et al., 2021) shortly after metaphase I into oocytes treated with U0126. As shown above, U0126 treatment prevents transition to MII, and oocytes exit after MI, form a pronucleus and enter parthenogenetic development (Fig 4D). Strikingly, injection of the active Cdk1-Cyclin B protein reverted effects of U0126: as in unperturbed meiosis, a second metaphase spindle formed without the formation of a nucleus (Fig 4D). However, likely due to the excess Cdk1-Cyclin B injected, oocytes then remained arrested at metaphase II in a 'CSF-like' state.

In conclusion, our data demonstrate that extra Cdk1-Cyclin B protein introduced shortly after meiosis I is sufficient to drive oocytes into the second meiotic division in the absence of Mos-MAPK activity, i.e. Cdk1-Cyclin B injection is sufficient to rescue the Mos-MAPK inhibition phenotype. Consistently, preventing Cyclin B synthesis by morpholino injection and general translation inhibition have similar effects to Mos-MAPK inhibition. These data together imply that Mos-MAPK activity drives the second meiotic division primarily by triggering translation of extra Cyclin B at the meiosis I to II transition.

Mos-MAPK regulates the size of centrosomal asters

That Mos-MAPK activity affects the asymmetry of meiotic divisions had been recognized early on, and since then shown in several species (Dupré et al., 2011). However, one caveat is that, as we show above, Mos-MAPK inhibition also affects the timing of divisions that complicates interpretation of data from oocytes fixed at specific time points. For example, we show here that Mos-MAPK inhibition abolishes MII, and thus a mitotic spindle forms following MI, which may have been misinterpreted as a delayed, abnormal MII spindle.

Therefore, we carefully correlated live recordings with fixed samples. This evidences that Mos-MAPK inhibition already affects the morphology of the meiosis I spindle. By contrast, inhibition of Cyclin B translation by morpholino (Fig 4A, B) or by general translation inhibition (Fig. 4D) did not affect the morphology of the MI spindle. This indicates that Mos-MAPK affects MI spindle morphology, and it does so independently of translational regulation.

To analyze effects on spindle organization in more detail, we recorded the first meiotic division in 3D at high spatial and temporal resolution in oocytes injected with recombinant EB3-mClover3 to label microtubule plus tips. We quantified the maximal length of the astral microtubules and the distance between the spindle poles at prophase, metaphase, anaphase, and telophase in DMSO- and U0126-treated oocytes. These analyses confirmed our previous observation of enlarged centrosomes in the U0126-treated metaphase I spindle, displaying longer astral microtubules and slightly increased pole-to-pole distance (Fig 5A-E). Strikingly, as cells

progressed into anaphase, the difference between control and U0126-treated spindles dramatically increased. In control spindles, astral microtubules and pole distance shortened as the division progressed. In stark contrast, in U0126-treated oocytes, asters and pole distance continued to increase as spindles progressed into anaphase and telophase (Fig. 5A-E). As visualized in Figure 5E, changes in the size of the asters and pole distances are tightly correlated, suggesting that the two processes may be functionally linked. Also consistent with the increased spindle and aster size, the size of the first polar body increased to approx. twice in diameter in Mos-MAPK inhibited oocytes as compared to control (Fig. 5F). Cytokinesis of these enlarged polar bodies frequently failed, and only 80% of Mos-MAPK inhibited oocytes completed polar body extrusion (Fig. 5G).

To complement these live-cell data, we also performed immunofluorescence stainings of spindles at these stages and recorded them in 3D at high-resolution (Fig. 6A). These data confirmed the striking difference in microtubule aster size and pole distance between control and Mos-MAPK inhibited oocytes as they progressed from metaphase to ana- and telophase. In quantifications, aster size and pole distance showed a large variability in prometaphase reflecting the dynamic changes during spindle assembly. While Mos-MAPK inhibition had a significant effect already at this stage, the difference was less than the variability within the samples (Fig. 6B-D). In metaphase, spindles are more uniform, but the difference between treated and control samples is still rather subtle at this stage (Fig. 6B-D). At anaphase and then telophase stages, the untreated spindle has very few astral microtubules, and spindle poles move towards each other, while chromosomes separate by shortening kinetochore fibers (Anaphase A). In stark contrast, Mos-MAPK inhibited oocytes display prominent microtubule asters, which contain much more microtubules and reach a size of ~20 µm towards telophase as compared to ~5 µm in controls (Fig. 6B-D). Increased centrosomal microtubule nucleation appears to be coupled to the formation of a prominent array of overlapping interpolar microtubules. The mid-spindle composed of this overlapping microtubule array mediates separation of spindle poles (Anaphase B) that is clearly observed in Mos-MAPK inhibited oocytes.

Taken together, our live cell and immunofluorescence data consistently show that Mos-MAPK specifically downregulates centrosomal microtubule nucleation most prominently in ana- and telophase and thereby critically contributes to minimizing polar body size. If Mos-MAPK is inhibited, the spindle adopts a mitotic-like morphology with astral microtubules pushing the spindle deeper into the cytoplasm, and promoting separation of spindle poles, resulting in enlarged polar bodies.

Discussion

Mos-MAPK acts as a switch to trigger the meiotic division program

Activation of the ERK/MAPK pathway by Mos is a conserved feature of oocyte meiotic divisions across animal species, controlling a number of key meiotic functions. However, downstream molecular targets of Mos-MAPK that underlie these functions are mostly unknown. Here, we took advantage of the transparent starfish oocytes available in large numbers to address this question by correlating cellular phenotypes monitored by live-cell microscopy with changes in the phosphoproteome analyzed by mass spectrometry.

Firstly, characterization of Mos-MAPK-inhibited oocytes by live cell imaging confirmed previous observations in starfish (Tachibana et al., 2000), and identified the metaphase of meiosis I as the critical transition. Mos-MAPK is activated at this point to mediate the highly asymmetric polar body divisions and triggers the reactivation of Cdk1-Cyclin B to drive the second meiosis. If Mos-MAPK is inhibited by U0126, the first meiotic division is less asymmetric and oocytes exit after meiosis I, re-form the nucleus, and start parthenogenetic embryo development.

Consistent with the cellular phenotypes, phosphoproteomic profiling of Mos-MAPK-inhibited oocytes in metaphase I revealed an overall signature of meiotic exit showing inactivation of Cdk1-Cyclin B and appearance of markers of interphase. Additionally, phosphoproteomics identified a

number of conserved molecular modules that mediate meiosis-specific functions downstream of Mos-MAPK. Specifically, we identified the modules regulating CPE-mediated translation, and cytoskeletal regulators involved in centrosomal microtubule nucleation, spindle organization as well as regulators of the actin cytoskeleton required for polar body cytokinesis.

Mos-MAPK mediates haploidization by triggering Cyclin B translation to drive meiosis II

Our data combined strongly supports the model, in which Mos-MAPK phosphorylates CPEB leading to the disassembly of the inhibitory complex formed by CPEB, Maskin/TACC3, and eIF4ENIF1. This then leads to the recruitment of the machinery responsible for polyadenylation of mRNAs and subsequent translation initiation. Overall, our hitlist included more than two-thirds of the subunits of these polyadenylation and translation initiation complexes. Interestingly, our top hits also included LARP1, a regulator specific to mRNAs with a 5' terminal oligopyrimidine (5'TOP). This motif is known to associate with the mTOR pathway (Berman et al., 2021), and it is intriguing to consider that this mechanism may play a role in meiotic regulation.

Translation of which mRNAs may be regulated by this mechanism? A recent phospho-proteomic survey of starfish oocyte meiosis showed that only a very limited number of proteins show a change in levels (Swartz et al., 2021). Indeed, the few changes detected are mostly proteins involved in the above translational pathway (e.g. CPEB and its regulators) and, prominently, Cyclin B (Swartz et al., 2021). Data from another starfish species also indicates that Cyclin B may be one of the very few if not the only protein translated during the MI to MII transition (Lapasset et al., 2008). Our experiments further support the critical role of Cyclin B translation in driving MII. Blocking Cyclin B translation has no detectable effect on MI, but it then causes oocytes to exit meiosis after MI, similar to Mos-MAPK inhibition. The same phenotype is observed after general translation inhibition by Emetine. Critically, we show that the effect of Mos-MAPK inhibition can be rescued by injection of the active Cdk1-Cyclin B protein. These strongly support the model, whereby Mos-MAPK triggers translation of Cyclin B at the MI-MII transition. This additional Cyclin B then reactivates Cdk1-Cyclin B to drive the second meiotic division, and to prevent entry into interphase (Fig. 7A).

This model is consistent with findings in several other species. Firstly, CPEB is highly conserved across animal species and has been shown to play critical roles in meiotic regulation. Specifically, the CPEB inhibitory complex was shown to regulate the translation of Cyclin B and is required for MI-to-MII transition in *Xenopus* oocytes (Hochegger et al., 2001; Arumugam et al., 2009). Additionally, in recent reports, Mos- MAPK was shown to facilitate Cyclin B translation by stimulating CPEB degradation in mouse oocytes (Cao et al., 2020). Our study identifies for the first time the specific subunits and their phosphorylation sites that link Mos-MAPK signaling to translational regulation.

While at the molecular level CPEB-mediated translational regulation is very well conserved, this is at odds with the substantial diversity in functions of Mos-MAPK observed at the cellular level. This diversity may be explained by changes in the temporal pattern of Cyclin B expression. For example, in *Xenopus* Mos-MAPK is required for meiotic maturation, because in this species the maturation hormone induces a translational response -- unlike the majority of species, including starfish, where the maturation hormone triggers a post-translational signaling cascade (Jessus et al., 2020). Correspondingly, in *Xenopus* Mos is translated directly in response to the maturation hormone, while in starfish Mos is first translated in metaphase I (Sheets et al., 1995; Tachibana et al., 2000). Similarly, despite the diversity of the CSF-like arrest points halting meiotic progression in MI, MII or G1 dependent on the species, these may use similar molecular mechanisms to maintain arrest by maintaining high levels of Cdk1-Cyclin B activity.

While translational regulation of Cyclin B certainly has a prominent role, additional transcripts may be under the control of the same regulation. There may indeed be a substantial species-to-species diversity in these evolved in adaptation to diverse reproductive strategies of different

species. It will be very exciting to sample this diversity by investigating transnational regulation in oocytes of diverse species.

Mos-MAPK facilitates asymmetric division by reducing the size of centrosomal microtubule asters

The other largest molecular module we identified are regulators of the microtubule cytoskeleton. These proteins fall into three categories: (i) constituents of the centrosome, and the pericentriolar material (PCM), (ii) regulators of microtubule growth at the plus-tips of microtubules, and (iii) kinesin motor proteins. While these proteins are not part of a single complex as the translational regulators, they do have a common function in organizing centrosomal microtubule arrays. Notably, our hits are rather specific in that we did not identify regulators of other major pathways in spindle organization, for example, those that depend directly on chromatin or are activated by chromatin-produced RanGTP (e.g. TPX2, HURP, or NuMA) (Valdez et al., 2023).

The cellular phenotypes are in excellent agreement with the functions of the identified phosphoproteins. Inhibition of Mos-MAPK renders the meiosis I spindle more 'mitotic' with larger centrosomal asters, and more numerous and longer astral microtubules. We show that compared to the relatively mild difference in prometa- and metaphase, Mos-MAPK inhibition has a much more dramatic effect during anaphase and telophase. Furthermore, while in normal meiosis chromosomes separate by shortening of the kinetochore fibers (anaphase A), in Mos-MAPK inhibited oocytes anaphase A and anaphase B, the separation of the spindle poles occurs in parallel -- as in mitotic divisions. Intriguingly, our data reveal a tight correlation between the maximal length of astral microtubules and pole-to-pole distance, suggesting that the two processes may be linked. The explanation for this can be that centrosomal microtubules grow in all directions, away from the spindle as astral microtubules, and into the spindle as interpolar microtubules. These interpolar microtubules may be critical to form the overlapping microtubule bundles at the spindle midzone that are then pushed apart in anaphase B by PRC1 and kinesin-4 (Bieling et al., 2010). In normal meiosis, with Mos-MAPK active, these interpolar microtubules are absent, and Anaphase B does not occur.

Mos-MAPK thus functions to minimize polar body size in two ways: by reducing aster size it allows the spindle to localize tightly to the cortex; and by preventing anaphase B, it limits the distance between the cortex and the spindle midzone (Fig. 7B). Thereby, Mos-MAPK basically switches off two mitotic spindle functions: positioning by astral microtubules, and anaphase B moving chromosome masses away from the cleavage furrow. This may in turn explain why oocytes employ specialized, actin-driven mechanisms for spindle positioning (Field and Lénárt, 2011).

Here we studied starfish oocytes, which have the unusual feature of retaining centrioles in meiotic divisions (Sluder et al., 1993; Borrego-Pinto et al., 2016a). This might make the above results somewhat more pronounced in starfish as compared to other species with acentrosomal meiotic spindles. However, acentrosomal microtubule organizing centers (aMTOCs) contain most if not all of the proteins we have identified, and functionally replace centriolar centrosomes in oocytes (Mogessie et al., 2018; Schuh and Ellenberg, 2007). Indeed, Mos-MAPK inhibition results in enlarged microtubule asters growing from aMTOCs in all species investigated so far, including *Xenopus*, mouse, and *Clytia* oocytes (Verlhac et al., 1996; Bodart et al., 2002; Amiel et al., 2009). Notably, in previous studies on fixed cells, the focus of observation has automatically been the relatively longer prometaphase and metaphase stages. We however showed that the effect of Mos-MAPK inhibition is most prominent in ana- and telophase. Therefore, it will be interesting to investigate ana- and telophase in other species as well. Indeed, although at low resolution, abnormal elongation of the anaphase spindle has already been observed in mouse Mos knockout oocytes (Verlhac et al., 2000).

Similarly to the translation module, the microtubule regulators we identified are widely conserved across animals, suggesting that regulation of centrosomes/aMTOCs and anaphase is another core conserved function controlled by Mos-MAPK. However, as for translation, there is

substantial diversity of meiotic spindle architectures among species. In some species centrosomes (e.g. starfish, (Burdyniuk et al., 2018) or aMTOCs (e.g. mouse, (Schuh and Ellenberg, 2007) play a substantial role in meiotic spindle organization, while in other species the chromosomal, Ran pathway dominates (e.g. human, (Holubcová et al., 2015). If our hypothesis is correct, we would predict that Mos-MAPK may have a stronger effect on spindles with dominant aMTOCs, while spindles that primarily depend on the Ran pathway may be less affected by Mos-MAPK.

Conclusions

Mos-MAPK and its functions in oocyte meiosis have been studied rather extensively in the past. These studies clearly evidence that Mos is an 'early invention' that has emerged before the split between cinarian and bilaterian species, and is thus an ancestral and conserved regulator of oocyte meiosis in animals. However, likely due to the inherent diversity of the cellular morphology and timing of oocyte meiosis among animal species, conserved molecular mechanisms under the control of Mos-MAPK have not been identified (Dupré et al., 2011). Here, by combining cellular studies with phosphoproteomics we revealed two highly conserved molecular modules controlled by Mos-MAPK: regulation of CPE-mediated translation and centrosomal microtubule nucleation. We show how these two modules mediate essential meiotic functions, driving haploidization and the highly asymmetric polar body divisions, respectively. While these modules may be activated at different times and adapted by other means in each species, their conservation strongly suggests that these core modules play critical roles in oocyte meiosis across metazoa.

Materials and Methods

Oocyte collection, drug treatments and microinjection

Bat stars (*Patiria miniata*) were obtained in the springtime from Southern California (South Coast Bio-Marine LLC, Monterey Abalone Company, or Marinus Scientific Inc). They were kept at 16 ˚C for the rest of the year in seawater aquariums at MPI-NAT's Animal Facility. Ovaries and testes were isolated as described previously (Borrego-Pinto et al., 2016b). Oocytes were isolated and used immediately or stored for 1-2 days in seawater at 14 ˚C, for some experiments ovaries were stored for 2-3 days in seawater at 14 ˚C and oocytes were isolated thereafter (Wessel et al., 2010).

mRNAs and other fluorescent markers were injected using Kiehart chambers and a horizontally mounted needles as described previously (Jaffe and Terasaki, 2004; Borrego-Pinto et al., 2016b), with the modification that instead of mercury-filled needles, simple back-loaded capillaries were used on a FemtoJet (Eppendorf) injector. mRNA was injected the day before to allow protein expression, whereas fluorescently labeled protein markers were injected just a few hours prior to imaging.

Meiosis was induced by the addition of 1-methyladenine (1-MA, Acros Organics) at 10 μM final concentration. NEBD started typically 20-25 min after 1-MA addition. U0126 (Sigma) was added simultaneously with 1-MA at 20 μM final concentration. Emetine (Sigma) was added at 100 μM final concentration 30 min before 1-MA. All compounds were dissolved in DMSO. For fertilization, freshly isolated sperm was added prior to the emission of the first polar body. Every experiment was repeated at least three times, with oocytes taken from at least two different animals.

Fluorescent and other markers

Chromosomes were labeled by either injecting mRNA encoding human H2B-mCherry or H1 protein purified from calf thymus (Sigma) labeled with AlexaFluor 568 or 647 as described

previously (Bun et al., 2018). Microtubules were labeled either by injection of HiLyte488- or HiLyte647-tubulin purified from the porcine brain (Cytoskeleton), or recombinant human EB3-mClover protein (a generous gift from So (Nick) Chun, Department of Meiosis, MPI-NAT, Göttingen, Germany). Anti-cyclin B morpholino TAACCAATGCGAGTTCCGAGGAG (Gene Tools), was injected at 500 mM final concentration immediately before 1-MA stimulation (Swartz et al., 2021).

Active Cdk1-Cyclin B complex was a generous gift from Pim J. Huis in't Veld and Andrea Musacchio (MPI for Molecular Physiology, Dortmund, Germany) (Veld et al., 2021). In order to remove glycerol, the complex was purified through a 10K MWCO protein concentrator (Pierce) and dissolved in PBS with 200 mM sucrose. The activity of the complex was confirmed by its ability to cause maturation in starfish oocytes . The Cdk1-Cyclin B complex was injected into the U0126-treated oocytes directly after the first polar body extrusion. Dynamics of labeled tubulin-HiLyte488 and H2B-mCherry were observed in U0126-treated and control oocytes simultaneously in the same injection chamber.

Capped mRNAs with poly-A tail were synthesized from linearized pGEMHE plasmids using the HiScribe™ T7 ARCA mRNA Kit (NEB). The mRNA was purified by Monarch RNA Cleanup Kit (NEB). Purified mRNAs were stored at 2-6 µg/µl concentration and were diluted prior to injection with Femtojet to 100-500 ng/µl.

Live cell microscopy

Starfish oocytes were imaged directly in the injection chambers. Live-cell images were acquired either on a Visitron Systems (Puchheim, Germany) spinning disk confocal microscope or on a Zeiss LSM780 (Jena, Germany) laser scanning confocal microscope. The spinning disk system is based on a Nikon Ti2 microscope body and a Yokogawa W1 scanhead and two Prime BSI cameras (Teledyne Photometrics). For live imaging experiments, a CFI SR Plan Apo IR 60x 1.27 NA water immersion objective was used. Typical settings for long-term imaging were: exposure time 200 ms, pixel size 110 nm, 11-15 z-slices with 3 or 4 µm step size, time intervals 3-5 min. On the laser scanning microscope, we used a C-Apochromat 40x 1.20 NA objective lens with the following settings: imaging area 100 µm × 100 µm, pixel size 200 nm, 15 z-slices with 2 µm step size, pinhole set to 2 AU, time intervals 3-5 min. Images of the control and experimental groups were acquired under identical imaging conditions on the same microscope.

Immunostaining

Oocytes were fixed at the desired times in a PFA/GA fixative (100 mM HEPES [pH 7.0], 50 mM EGTA, 10 mM $MgSO_4$, 0.5% Triton-X100, 400 mM Sucrose, 2% formaldehyde, 0.2% glutaraldehyde) modified from (Strickland et al., 2004). Subsequently, samples were permeabilized and blocked in blocking buffer (PBS+0.1% Triton-X100 plus 3% BSA and the Image-IT reagent (Thermo Scientific)). Antibody staining was done for 24 h in a blocking buffer at room temperature with the primary antibody premixed with secondary nanobodies/Fab fragment. Microtubules were labeled with anti-α-tubulin mouse antibody (clone DM1A) (Sigma), and lamin was labeled with a custom-made rabbit polyclonal antibody (Wesolowska et al., 2020) primarily labeled with Alexa 488 NHS ester (Thermo Scientific) according to the manufacturer's instructions. Secondary staining was done by anti-mouse secondary nanobodies with Atto-488 (NanoTag) or donkey Fab anti-mouse IgG AlexaFluor594 (Jackson). DNA was labeled with Hoechst 33342 (Thermo Scientific). Oocytes were mounted with the antifade agent ProLong Glass or SlowFade Diamond (Thermo Scientific) on a coverslip pressed gently onto drops of silicone grease or double-sided tape (Scotch). Fixed oocytes were imaged on the same microscope systems as used for live imaging with the following modifications: for the spinning disk confocal microscope, exposure time of 200 ms, pixel size of 110 nm, and 70 z-slices with 200 or 600 nm step size. On the laser scanning system we used a pixel size of 40 nm, 80 z-slices with 200 nm step size, pinhole set to 1 Airy unit.

Image analysis

Prior quantification, immunofluorescent images were deconvolved using the Huygens software (Scientific Volume Imaging) with either confocal, AiryScan, or spinning disk settings as appropriate. Quantification was done in ImageJ/FIJI (Schindelin et al., 2012). Images were rotated and resliced in XY and XZ planes to orient the spindle orthogonally. The quantification of spindle length, spindle width, and diameter of centrosomes were done by measuring the half-maximal width of the intensity profile along the respective structures along the spindle axis. Statistical analysis was performed by Excel (Microsoft), results were plotted in R (R Core Team).

The maximal length of microtubules and spindle diameter were quantified on live images using ImageJ/FIJI (Schindelin et al., 2012) in a maximal Z-projected volume slab of 10 µm thickness. The maximal length of microtubules was estimated by measuring the distance of aster tips to the centriole (both labeled by EB3-mClover) and the pole distance was measured by placing points at each pole and calculating their 3D distance. Statistical analysis was performed by using Excel (Microsoft), results were plotted in R (R Core Team).

For presenting images on figures, we typically used a Gaussian blur of 0.5-1 pixels to reduce shot noise. Images were adjusted for brightness and contrast, and where indicated, gamma adjustments were applied.

Sample preparation and LC/MS analysis

For a detailed protocol see Supplemental Material. Three biological replicates of oocytes were collected from three different starfish animals. Oocytes were matured by addition of 1-MA and collected at metaphase I. Synchronicity of oocytes was confirmed by staining a small portion of the collected oocytes with Hoechst 33342. In these samples, we could observe a metaphase plate in 92-96% of the oocytes by confocal microscopy.

20 µl of starfish oocytes were lysed on ice, and ruptured by centrifuging the oocyte suspension through a 40 µm plastic mesh at 7000 g. Sample cleanup was performed by applying a single-pot, solid-phase-enhanced sample preparation protocol by (Hughes et al., 2019). Aliquots were taken for whole proteome analysis, and the rest of the sample was subjected to phosphopeptide enrichment using the EasyPhos protocol (Humphrey et al., 2015). TMTsixplex™ (Thermo Scientific) labeling was performed according to manufacturer's instructions. Whole proteome and phosphopeptide-enriched samples were labeled separately and combined in separate samples.

Whole proteome and phosphopeptide samples were dissolved in 2% [v/v] ACN 0.1% [v/v] TFA and injected onto a C18 PepMap100-trapping column (0.3 x 5 mm, 5 µm, Thermo Scientific) connected to an in-house packed C18 analytical column (75 µm x 300 mm; Reprosil-Pur 120C18-AQ, 1.9 µm, Dr Maisch GmbH). Liquid chromatography was performed using an UltiMate-3000 RSLC nanosystem (Thermo Scientific). Eluting peptides were analyzed on an Orbitrap Exploris 480 instrument (Thermo Scientific).

The mass spectrometry proteomics data have been deposited to the ProteomeXchange Consortium via the PRIDE (Perez-Riverol et al., 2022) partner repository with the dataset identifier PXD043650.

Reference proteome annotation and proteomics data analysis

For detailed description see Supplemental Material. In brief, the protein database was compiled using datasets at Echinobase v2 (echinobase.org) (Kudtarkar and Cameron, 2017) and NCBI annotation (RefSeq ID 23626818) for *Patiria miniata*. Protein-coding transcripts with reduced redundancy were annotated *via* TRAPID web interface [TRAPID] using EggNOG 4.5.1 database (Huerta-Cepas et al., 2016).

Raw mass spectrometry files were processed using MaxQuant version 1.6.17.0 (Cox and Mann, 2008). MaxQuant output tables were filtered to remove decoys and contaminants. Ratios of phospho-peptide intensities from “modificationSpecificPeptides” table to the corrected intensities of their parent proteins were log2-transformed and used for subsequent differential expression analysis. A linear model testing for the difference between means of phospho-peptide ratios in treatment and control groups were fit with least-squares, and p-values were estimated with the empirical Bayes approach. Multiple hypothesis correction was done using the Benjamini and Hochberg approach for false discovery rate (FDR) estimation. In addition, q-values were used to inform the significance cutoff choice, which was set to the adjusted p-value of 0.07.

Functional enrichment analysis was performed using the g:Profiler tool g:GOSt. Normalized ratios of significantly up- and down- regulated phosphopeptides were scaled to the mean of 0 and standard deviation of 1. In order to cluster the results by magnitude of differential expression and functional annotation, each peptide was checked for originating from a protein belonging to the following functional terms: "cytoskeleton", "microtubule cytoskeleton", "spindle", "cell cycle”, “regulation of protein kinase activity”, “dephosphorylation” and a matrix with binary indicators was bound to columns to the scaled phospho-peptide intensity matrix. Euclidean distance between peptides in this matrix was used for hierarchical clustering. MaxQuant’s "evidence" table was used to extract the “Phospho (STY) Probabilities” for each peptide-spectrum match (PSM). A mean probability per amino acid across all PSMs with the same peptide sequence was computed and the maximal value per peptide sequence was used to estimate the most likely position of phosphorylation. Peptide sequences, log-fold changes and p-values of differential expression were submitted for kinase prediction at phosphosite.org (Hornbeck et al., 2015).

Acknowledgements

We thank all members of the Lenart laboratory at MPI-NAT for protocols, reagents and support, in particular Jasmin Jakobi and Antonio Politi. We thank MPI-NAT’s Animal Facility, specifically Sascha Krause and Ulrike Teichmann. We would like to thank So (Nick) Chun and Melina Schuh for providing the recombinant EB3-mClover3 protein, Pim J Huis In't Veld and Andrea Musacchio for Cdk1-Cyclin B complex and Dirk Görlich for Gibson assembly kit. I.A. is a member and has been partially funded by the IMPRS Molecular Biology Programme. The laboratory is funded by the Max Planck Society.

Competing interests

The authors declare no competing financial interests.

Figure legends

Figure 1. Inhibition of Mos-MAPK activity prevents entry into the second meiosis and causes oocytes to progress without arrest to parthenogenetic development

(A) Selected frames from a time-lapse recording of oocytes expressing H2B-mCherry (red) and injected with HiLyte488-tubulin (cyan) to label chromosomes and microtubules, respectively. Oocytes were imaged through meiosis and then fertilized after meiosis I while imaging on a spinning disk confocal microscope. Before inducing maturation, oocytes were treated either with 20 μM U0126 or an equal amount of DMSO. Maximum intensity projections are shown, scale bars are 20 μm, and time is given as mm:ss. Arrows indicate the polar bodies. Venus and Mars signs indicate female and male pronuclei respectively.

(B) Boxplot showing the time from nuclear envelope breakdown (NEBD) to metaphase I quantified on recordings similar to shown in (A). Statistical comparison was done using the Mann-Whitney test.

(C) Boxplot showing the time from meiotic metaphase I to the first mitotic metaphase quantified on recordings similar to those shown in (A). Statistical comparison was done using the Mann-Whitney test.

(D) Immunofluorescence images of oocytes stained for microtubules (anti-tubulin, blue), chromatin (Hoechst 33342, red), and the lamina (anti-lamin B, green). Oocytes were treated with 20 μM U0126 or an equal amount of DMSO and then fixed 60 and 120 minutes after inducing maturation, respectively. Samples were imaged on a spinning disk microscope. Maximum intensity projections are shown, scale bars are 20 μm.

(E) Immunofluorescence images of oocytes stained for microtubules (anti-tubulin antibody, blue) and chromatin (Hoechst 33342, red) at the indicated stages and treated with 20 μM U0126 or an equal amount of DMSO. Imaging was done on a laser scanning confocal microscope. Maximum intensity projections are shown, scale bars are 20 μm.

(F) Schematics of the meiotic spindle illustrating the carried-out measurements. Microtubules are blue and chromatin is red.

(G) Boxplots showing 3D measurements performed on images similar to those shown in (E) and as illustrated in (B). **$p<0.05$, ***$p<0.0001$. Statistical analysis was done using a two-tailed T-test.

Figure 2. Phospho-proteomics of metaphase I oocytes reveals cell cycle regulation, cytoskeleton and translation as the most prominent processes regulated by Mos-MAPK

(A) Outline of the phospho-proteomics experiment. Mos-MAPK-inhibited (purple) and control (green) oocytes were collected at metaphase I in three biological replicates. Phosphopeptides were enriched prior to TMT labeling. Enriched and non-enriched samples were analyzed by MS2.

(B) Overall statistics representing proteins and phospho-peptides identified and quantified.

(C) Unsupervised clustering of differentially phosphorylated peptides (rows) vs TMT channels (columns) confirms the effect of treatment above biological variability. Green: control, Purple: Mos-MAPK inhibition. Heatmap is scaled to Log2 fold-changes and to mean of 0 and SD of 1.

(D) Gene ontology enrichment analysis of differentially phosphorylated proteins identifies cell cycle regulation and cytoskeleton as the main processes regulated by Mos-MAPK activity.

(E) Prediction of human effector kinase families enriched in the differentially phosphorylated peptides. For complete data see Supplementary File 3.

(F) Volcano plot of the quantified phosphopeptides. The majority of phosphopeptides were manually classified into four categories: Translation, Cytoskeleton, Cell cycle regulation, and MAPK pathway. The rest of the phosphopeptides including those from unidentified proteins are marked as gray dots. For data see Supplementary File 1 and 2.

Figure 3. Phosphoproteomics identifies functional molecular modules regulated by Mos-MAPK activity

(A) The functional modules were manually selected from the list of significantly affected phosphopeptides (Supplementary File 1 and 2). Color code indicates Log2 fold change in phosphopeptide abundance upon Mos-MAPK inhibition.

(B) The modules indicated in (A) grouped and schematized according to functional relation to each other. Color coding represents the Log2 fold change in phosphopeptide abundance upon Mos-MAPK inhibition.

Figure 4. Translation of extra Cyclin B is sufficient to drive the second meiotic division

(A) Selected frames from a time-lapse recording of oocytes injected with H1-Alexa647 (red) and HiLyte488-tubulin (cyan) to label chromosomes and microtubules, respectively. Oocytes were imaged through meiosis on a spinning disk confocal microscope. Before inducing maturation, oocytes were injected with either a morpholino targeting Cyclin B or water as control. Maximum intensity projections are shown, scale bars are 20 μm, and time is given as mm:ss. PB I and II denote the first and second polar bodies, respectively; PN is the pronucleus.

(B) Boxplot showing a comparison of the maximal length of microtubules at metaphase I between control oocytes and oocytes injected with Cyclin B morpholino. Statistical comparison was done using a two-tailed T-test.

(C) Selected frames from a time-lapse recording of an oocyte injected with H1-Alexa647 (red) and HiLyte488-tubulin (cyan) to label chromosomes and microtubules, respectively. The oocyte was imaged through meiosis on a spinning disk confocal microscope. Before inducing maturation, the oocyte was treated with 100 μM Emetine to block translation. Maximum intensity projections are shown, the scale bar is 20 μm, and time is given as mm:ss. PB I denotes the first polar body, and PN is the pronucleus.

(D) Selected frames from a time-lapse recording of oocytes expressing H2B-mCherry (red) and injected with HiLyte488-tubulin (cyan) to label chromosomes and microtubules, respectively. Oocytes were imaged through meiosis on a spinning disk confocal microscope. Before inducing maturation, oocytes were treated with 20 μM U0126. Then oocytes were either left unmanipulated or they were injected with active Cdk1-Cyclin B protein immediately following extrusion of the first polar body. Maximum intensity projections are shown, scale bars are 20 μm, and time is given as mm:ss. PB I denotes the first polar body, and PN is the pronucleus.

Figure 5. Mos-MAPK activity reduces aster size and prevents spindle elongation, minimizing polar body size

(A) Selected frames from a time-lapse recording of the microtubule spindle in an oocyte undergoing meiosis I on a spinning disk confocal microscope. Chromosomes are labeled with H1-Alexa568 (red) and microtubule plus tips by EB3-mClover3 protein (cyan). Before inducing maturation, the oocyte was treated with either 20 μM U0126 or an equal amount of DMSO. (left) overlay of the two fluorescent channels; (middle) the EB3-mClover3 channel is shown with adjusted gamma; (right) 3D rendering of the centrosome (cyan) and chromosomes (red). Maximum intensity projections are shown, and scale bars are shown in μm.

(B) 3D distances of the spindle poles (inclusive centrosomes) at different stages of meiosis I quantified on recording similar to (A).

(C) The maximal length of astral microtubules quantified at different stages of meiosis I quantified on recording similar to (A).

(D) Illustration of correlated changes in aster size and pole distance. Mean values shown on (B) and (C) are plotted on schematics of the spindle.

(E) Boxplot showing quantification of polar body sizes ***p<0.0001. Statistical comparison was done using a two-tailed T-test.

(F) Bar chart showing the rate of polar body formation. Polar bodies were counted by live imaging in H1-Alexa568-injected oocytes after completion of meiosis.

Figure 6. Mos-MAPK activity reduces centrosomal microtubule nucleation

(A) Immunofluorescence images of oocytes stained for microtubules (anti-tubulin, cyan), and chromatin (Hoechst 33342, red). Oocytes were treated with 20 µM U0126 or an equal amount of DMSO, and then fixed at the stages indicated. Imaging was done using spinning disk confocal microscopy. Maximum intensity projections are shown, scale bar is 20 µm. Lower panels show the tubulin channel separately and with adjusted gamma (0.5).

(B) Quantification of the maximal length of astral microtubules on data similar to shown in (A). **p<0.05, ***p<0.0001 in two-tailed t-tests.

(C) Quantification of the 3D distance of spindle poles on data similar to shown in (A). **p<0.05, ***p<0.0001 in two-tailed T-tests.

(D) Single optical sections crossing the centrosomes selected from the projected images shown in (A). Images are shown after gamma adjustment (0.5).

Figure 7. Model for regulation of oocyte meiosis by Mos-MAPK

(A) Top: schematics of Mos-MAPK and Cdk1 activity changes through meiotic and mitotic divisions. Bottom: schemes of steps of oocyte meiosis and subsequent mitotic divisions in untreated oocytes with Mos-MAPK active and in U0126-treated oocytes with Mos-MAPK activity inhibited.

(B) Mos-MAPK specifically downregulates pericentriolar material proteins, reduces the growth as well as the amount of astral and interpolar microtubules, and prevents Anaphase B. This allows close attachment of the meiotic spindle to the oocyte cortex in order to complete the division as compactly as possible, resulting in an extremely asymmetric cell division, the extrusion of the polar body.

Supplementary material

Supplementary Materials and Methods

Sample preparation for mass spectrometry

We collected three biological replicates of starfish oocytes at the metaphase I stage, following treatment with the maturation hormone, 1-MA. The synchronicity of oocytes was confirmed by staining a small portion of the collected oocytes with Hoechst 33342. For the samples used for further analysis, we observed a metaphase plate in 92-96% of the oocytes by confocal microscopy.

20 µl of starfish oocytes were lysed on ice in SDS lysis buffer (4% [w/v] SDS, 150 mM Hepes-KOH pH 7.0, 2 mM dithiothreitol (DTT), 10 mM EDTA, 250 mM sucrose), buffer containing a protease inhibitor cocktail (Complete Roche Mini). The mechanical cell disruption was done by centrifuging the oocyte suspension through 40 µm plastic mesh at 7000 g. Samples were diluted to a final 0.1% SDS and 1 mM $MgCl_2$ was added. Proteins were reduced with 5 mM DTT for 30 min at 37°C, 300 rpm, and alkylated with 10 mM iodoacetamide (IAA) for 30 min at 25°C, 300 rpm, in the dark. The reaction was quenched with 10 mM DTT for 5 min at 25°C, 300 rpm.

Sample cleanup was performed by applying a single-pot, solid-phase-enhanced sample preparation protocol by (Hughes et al., 2019). Briefly, carboxylate-modified magnetic beads (Cytiva 65152105050350, 45152105050250, mixed 1:1) were added at a 1:10 protein-to-bead mass ratio with an equal volume of 100% [v/v] acetonitrile (ACN). Beads were washed twice with 80% [v/v] EtOH and once with 100% [v/v] ACN. Proteins were digested in 50 mM TEAB containing trypsin (Promega, V5111) at a 1:20 enzyme-to-protein ratio overnight at 37 °C, 1000 rpm. Peptides were removed from the magnetic beads and aliquots were taken for whole proteome analysis.

Residual samples were subjected to phosphopeptide enrichment according to the EasyPhos protocol (Humphrey et al., 2015). Briefly, peptide mixtures were adjusted to final 228 mM KCl, 3.9 mM KH_2PO_4, 38% [v/v] ACN, 4.5% [v/v] trifluoroacetic acid (TFA), mixed and cleared by centrifugation. TiO_2 beads (GL Sciences, 5010-21315, 10 µm) in 80% ACN, 6% TFA were added at a beads-to-protein ratio of 10:1. Peptides were incubated with beads for 20 min at 40°C, 1000 rpm. Beads were resuspended and washed in 60% [v/v] ACN, 1% [v/v] TFA four times. Finally, beads were resuspended in 80% [v/v] ACN, 0.5% [v/v] acetic acid and transferred to empty columns (Harvard Apparatus, 74-3840). Phosphopeptides were eluted in two steps with 40% [v/v] ACN, 15% [v/v] NH_4OH.

TMTsixplex™ (Thermo Scientific, 90061) labeling was performed according to manufacturer's instructions. Whole proteome and phosphopeptide-enriched samples were labeled separately. Both were further cleaned using C18 MicroSpin columns (Harvard Apparatus, 74-4601) according to manufacturer's instructions. Samples were dissolved in 10 mM NH_4OH pH 10, 5% [v/v] ACN and peptides were loaded onto an Xbridge C18 column (Waters, 186003128) using an Agilent 1100 series chromatography system. The column was operated at a flow rate of 60 µl/min with a buffer system of buffer A, 10 mM NH_4OH pH 10; and buffer B, 10 mM NH_4OH pH10, 80% [v/v] ACN. The column was equilibrated with 5% B and separation was performed over 64 min using the following gradient: 5% B (0-7 min), 8-30% B (8-42 min), 30-50% B (43-50 min), 90-95% B (51-56 min), 5% B (57-64 min). For phosphopeptides, the first 6 min were collected as flow-through (FT), followed by 48 x 1 min fractions, which were reduced to 23 fractions by concatenated pooling. The remaining fractions were discarded. For the whole proteome sample, 54 x 1 min fractions were collected and combined to 19 final fractions. The remaining fractions were discarded. Fractionated whole proteome and phosphopeptide samples were dried in a speed vac concentrator and subjected to LC-MS/MS analysis.

LC-MS/MS analysis

Whole proteome and phosphopeptide samples were dissolved in 2% [v/v] ACN 0.1% [v/v] TFA and injected onto a C18 PepMap100-trapping column (0.3 x 5 mm, 5 µm, Thermo Scientific) connected to an in-house packed C18 analytical column (75 µm x 300 mm; Reprosil-Pur 120C18-AQ, 1.9 µm, Dr Maisch GmbH). Columns were equilibrated using 8% buffer A (0.1% [v/v] formic acid (FA)), 2% buffer B (80% [v/v] ACN, 0.1% [v/v] FA) (phosphopeptides), or 95% buffer A, 5% buffer B (whole proteome peptides). Liquid chromatography was performed using an UltiMate-3000 RSLC nanosystem (Thermo Scientific). Phosphopeptides were analyzed for 88 min using a linear gradient (10% to 30% buffer B (80% [v/v] ACN, 0.1% [v/v] FA) in 60 min) followed by a linear increase to 40% buffer B over 10 min and a 5 min washing step at 90% of buffer B. Whole proteome peptides were analyzed for 88 min, and a buffer B gradient of 10% to 45% over 60 min was applied followed by a linear increase to 60% buffer B over 10 min and washing at 90% buffer B for 5 min.

Eluting peptides were analyzed on an Orbitrap Exploris 480 instrument (Thermo Scientific). For the analysis of phosphopeptides, the following MS settings were used: MS1 scan range, 350–1600 *m/z*; MS1 resolution, 120,000 FWHM; AGC target MS1, 3E6; maximum injection time MS1, 50 ms; isolation window, 1.6 *m/z*; collision energy, 34%; charge states, 2+ to 6+; dynamic exclusion, 25 s; MS2 resolution, 30,000, AGC target MS2, 1e5; maximum injection time MS2, 64 ms. For the analysis of whole proteome peptides, the following MS settings were used: MS1 scan range, 350–1600 *m/z*; MS1 resolution, 60,000 FWHM; AGC target MS1, 3E6; maximum injection time MS1, 50 ms; isolation window, 0.8 *m/z*; collision energy, 34%; charge states, 2+ to 6+; dynamic exclusion, 25 s; MS2 resolution, 15,000, AGC target MS2, 5e4; maximum injection time MS2, 54 ms.

The mass spectrometry proteomics data have been deposited to the ProteomeXchange Consortium via the PRIDE (Perez-Riverol et al., 2022) partner repository with the dataset identifier PXD043650.

Reference proteome annotation

Two available different sources of genomic information were integrated together: Echinobase v2 and NCBI annotation for *Patiria miniata*. First, protein sequencers from both sources were clustered together to identify representative sequences using mmseqs2 [Linclust] easy-clust workflow with a sequence similarity threshold of 0.95 (-c flag).

Transcript sequences for Echinobase v2 were derived from the genome sequence and transcriptome annotation in gff format with gffread [gffread] software with -M and -K flags in order to discard duplicate transcripts and transcripts fully contained in other longer sequences.

Transcript sequences were extracted from both transcriptomes that correspond to proteins marked as representative sequences by mmseqs2 using a custom R script.

A set of protein-coding transcripts with reduced redundancy was annotated via TRAPID web interface [TRAPID] using EggNOG 4.5.1 database. Full log of TRAPID annotation is provided in the Supplementary Data at https://doi.org/10.25625/03K7BQ. KEGG ontology gene names were used as a main annotation; in case of their absence NCBI names were used, and in when neither of the above was available – Echinobase v2 identifiers were kept. Gene ontology and KEGG ontology identifiers were downloaded and formatted into a GMT format file to be used as functional annotation sets for over-representation analysis.

Differential protein expression analysis

MS raw files were processed using MaxQuant version 1.6.17.0 (Cox and Mann, 2008) with default settings except for: fixed modification, carbamidomethylation (C); variable modifications, oxidation (M), acetylation (N-term), phosphorylation (S,T,Y) (only for phosphopeptide data); enzyme, trypsin/P digestion. MS2 (TMTsixplex™) was selected as the quantification type.

A "proteinGroups" table with corrected reporter ion intensities from MaxQuant was used for differential expression. After removing contaminants and decoys, proteins with Q-value of

detection <= 0.01 and with at least 1 unique peptide were kept for further analysis. We made a choice of requiring only 1 unique peptide in order to evaluate the differential expression of MOS kinase, that would have been filtered out otherwise.

Reporter ion intensities were log2-transformed and linear models were fit using least squares method from limma R library [limma]. P-values were estimated with the empirical Bayes method and multiple hypothesis testing correction was done with the Benjamini and Hochberg method [padj BH]. A significance cutoff of 0.05 adjusted p-value was used.

Differential phosphoproteomics analysis

MaxQuant output tables were filtered to remove decoys and contaminants. All peptides with posterior error probability (PEP) <= 0.01 were kept. Protein groups did not undergo additional filtering by Q-value or number of unique peptides, in order to preserve the most proteins possible for downstream normalization of phospho-peptide intensities. Missing values in corrected TMT reporter intensities of all total protein in "proteinGroups" table were imputed conservatively, with minimal reporter intensity per channel.

Ratios of phospho-peptide intensities from "modificationSpecificPeptides" table to the corrected intensities of their parent proteins were log2-transformed and used for subsequent differential expression with limma [limma]. Overall, 76% of phospho-peptides had a corresponding total protein intensity necessary for normalization. A linear model testing for the difference between means of phospho-peptide ratios in treatment and control groups were fit with least-square approach and p-values were estimated with empirical Bayes approach. Multiple hypothesis correction was done with Benjamini and Hochberg for false discovery rate (FDR) estimation [padj_BH]. In addition, q-values were used to inform the significance cutoff choice [qvalue] which was set to adjusted p-value (BH) of 0.07.

Functional enrichment of differential phosphorylation analysis

Gene list functional enrichment was performed using g:Profiler tool g:GOSt [g:Profiler]. Three sets of gene names corresponding to up-regulated, down-regulated and all significant hits were enriched using a default "g_SCS" correction method and a significance threshold of 0.05. A functional annotation from TRAPID was uploaded to the web-server of g:Profiler and used as an organism specific reference (organism "gp__EGla_34PO_4UY").

Heatmap of differential phosphorylation

Normalized ratios of significantly up- and down- regulated phospho-peptides were scaled to the mean of 0 and standard deviation of 1. In order to cluster the results by magnitude of differential expression and functional annotation, each peptide was checked for originating from a protein belonging to the following functional terms: "cytoskeleton", "microtubule cytoskeleton", "spindle", "cell cycle", "regulation of protein kinase activity", "dephosphorylation" and a matrix with binary indicators (1 for match, 0 for mismatch) was bound to columns to the scaled phospho-peptide intensity matrix. Euclidean distance between peptides in this matrix underwent hierarchical clustering with "ward.D2" method (Murtagh and Legendre, 2014). to minimize the squared variance within clusters. Heatmap was plotted using "pheatmap"[pheatmap] R package with default settings and row order from the abovementioned clustering.

Prediction of effector human kinases

MaxQuant "evidence" table was used to extract the `Phospho (STY) Probabilities` for each peptide-spectrum match (PSM). A mean probability per amino acid across all PSMs with the same peptide sequence was computed and the maximal value per peptide sequence was used to estimate the most likely position of phosphorylation. All the peptides tested for differential expression, including insignificant hits were converted to the asterisk format, where the phosphorylated amino acid is marked with an asterisk (*) after the phospho-acceptor (S, T, Y). Peptide sequences, log-fold changes and p.values of differential expression were submitted for kinase prediction at phosphosite.org (Hornbeck et al., 2015) kinaseLibraryAction functional enrichment analysis based on differential expression. P-value threshold of 0.05 was used to discriminate between foreground and the background sets.

Supplementary Files

Supplementary File 1

Results of the differential expression analysis (DEA) of the ratios of phosphorylated peptides to their total protein intensities in U0126 versus DMSO treated samples.

Supplementary File 2

Results of the manual annotation of the significant hits (p-adj>0.05) from the differential expression analysis (DEA).

Supplementary File 3

Results of the putative human protein kinases prediction obtained from analysis of all phospho-peptides tested for differential expression with PhosphoSitePlus.

References

Abrieu, A., M. Dorée, and D. Fisher. 2001. The interplay between cyclin-B-Cdc2 kinase (MPF) and MAP kinase during maturation of oocytes. *J. Cell Sci.* 114:257–267. doi:10.1242/jcs.114.2.257.

Amiel, A., L. Leclère, L. Robert, S. Chevalier, and E. Houliston. 2009. Conserved Functions for Mos in Eumetazoan Oocyte Maturation Revealed by Studies in a Cnidarian. *Curr. Biol.* 19:305—311. doi:10.1016/j.cub.2008.12.054.

Araki, K., K. Naito, S. Haraguchi, R. Suzuki, M. Yokoyama, M. Inoue, S. Aizawa, Y. Toyoda, and E. Sato. 1996. Meiotic Abnormalities of c-mos Knockout Mouse Oocytes: Activation after First Meiosis or Entrance into Third Meiotic Metaphase. *Biol. Reprod.* 55:1315–1324. doi:10.1095/biolreprod55.6.1315.

Arumugam, K., Y. Wang, L.L. Hardy, M.C. MacNicol, and A.M. MacNicol. 2009. Enforcing temporal control of maternal mRNA translation during oocyte cell-cycle progression. *EMBO J.* 29:387–397. doi:10.1038/emboj.2009.337.

Bendre, S., A. Rondelet, C. Hall, N. Schmidt, Y.-C. Lin, G.J. Brouhard, and A.W. Bird. 2016. GTSE1 tunes microtubule stability for chromosome alignment and segregation by inhibiting the microtubule depolymerase MCAK. *J. Cell Biol.* 215:631–647. doi:10.1083/jcb.201606081.

Berman, A.J., C.C. Thoreen, Z. Dedeic, J. Chettle, P.P. Roux, and S.P. Blagden. 2021. Controversies around the function of LARP1. *RNA Biol.* 18:207–217. doi:10.1080/15476286.2020.1733787.

Bhatt, R.R., and J.E. Ferrell. 1999. The protein kinase p90 rsk as an essential mediator of cytostatic factor activity. *Science*. 286:1362–1365. doi:10.1126/science.286.5443.1362.

Bieling, P., I.A. Telley, and T. Surrey. 2010. A Minimal Midzone Protein Module Controls Formation and Length of Antiparallel Microtubule Overlaps. *Cell*. 142:420–432. doi:10.1016/j.cell.2010.06.033.

Bodart, J.-F.L., D.V. Gutierrez, A.R. Nebreda, B.D. Buckner, J.R. Resau, and N.S. Duesbery. 2002. Characterization of MPF and MAPK Activities during Meiotic Maturation of Xenopus tropicalis Oocytes. *Dev. Biol.* 245:348–361. doi:10.1006/dbio.2002.0647.

Borrego-Pinto, J., K. Somogyi, M.A. Karreman, J. König, T. Müller-Reichert, M. Bettencourt-Dias, P. Gönczy, Y. Schwab, and P. Lénárt. 2016a. Distinct mechanisms eliminate mother and daughter centrioles in meiosis of starfish oocytesCentriole elimination in starfish oocytes. *J. Cell Biol.* 212:815–827. doi:10.1083/jcb.201510083.

Borrego-Pinto, J., K. Somogyi, and P. Lénárt. 2016b. Oogenesis, Methods and Protocols. *Methods Mol. Biol.* 1457:145–166. doi:10.1007/978-1-4939-3795-0_11.

Bourdais, A., B. Dehapiot, and G. Halet. 2023. MRCK activates mouse oocyte myosin II for spindle rotation and male pronucleus centration. *J. Cell Biol.* 222:e202211029. doi:10.1083/jcb.202211029.

Bun, P., S. Dmitrieff, J.M. Belmonte, F.J. Nédélec, and P. Lénárt. 2018. A disassembly-driven mechanism explains F-actin-mediated chromosome transport in starfish oocytes. *eLife*. 7:e31469. doi:10.7554/elife.31469.

Burdyniuk, M., A. Callegari, M. Mori, F. Nédélec, and P. Lénárt. 2018. F-Actin nucleated on chromosomes coordinates their capture by microtubules in oocyte meiosis. *J. Cell Biol.* 217:2661–2674. doi:10.1083/jcb.201802080.

Cao, L.-R., J.-C. Jiang, and H.-Y. Fan. 2020. Positive Feedback Stimulation of Ccnb1 and Mos mRNA Translation by MAPK Cascade During Mouse Oocyte Maturation. *Front. Cell Dev. Biol.* 8:609430. doi:10.3389/fcell.2020.609430.

Church, D.L., K.L. Guan, and E.J. Lambie. 1995. Three genes of the MAP kinase cascade, mek-2, mpk-1/sur-1 and let-60 ras, are required for meiotic cell cycle progression in Caenorhabditis elegans. *Dev. Camb. Engl.* 121:2525–2535. doi:10.1242/dev.121.8.2525.

Colledge, W.H., M.B.L. Carlton, G.B. Udy, and M.J. Evans. 1994. Disruption of c-mos causes parthenogenetic development of unfertilized mouse eggs. *Nature*. 370:65—68.

doi:10.1038/370065a0.
Conduit, P.T., A. Wainman, and J.W. Raff. 2015. Centrosome function and assembly in animal cells. *Nat. Rev. Mol. Cell Biol.* 16:611–624. doi:10.1038/nrm4062.
Cox, J., and M. Mann. 2008. MaxQuant enables high peptide identification rates, individualized p.p.b.-range mass accuracies and proteome-wide protein quantification. *Nat. Biotechnol.* 26:1367–1372. doi:10.1038/nbt.1511.
Dumollard, R., M. Levasseur, C. Hebras, P. Huitorel, M. Carroll, J.-P. Chambon, and A. McDougall. 2011. Mos limits the number of meiotic divisions in urochordate eggs. *Dev. Camb. Engl.* 138:885–895. doi:10.1242/dev.057133.
Dumont, J., M. Umbhauer, P. Rassinier, A. Hanauer, and M.-H. Verlhac. 2005. p90Rsk is not involved in cytostatic factor arrest in mouse oocytes. *J. Cell Biol.* 169:227–231. doi:10.1083/jcb.200501027.
Dupré, A., O. Haccard, and C. Jessus. 2011. Mos in the Oocyte: How to Use MAPK Independently of Growth Factors and Transcription to Control Meiotic Divisions. *J. Signal Transduct.* 2011:350412. doi:10.1155/2011/350412.
Field, C.M., and P. Lénárt. 2011. Bulk cytoplasmic actin and its functions in meiosis and mitosis. *Curr. Biol. CB*. 21:R825-830. doi:10.1016/j.cub.2011.07.043.
Fukasawa, K., and G.F.V. Woude. 1995. Mos overexpression in Swiss 3T3 cells induces meiotic-like alterations of the mitotic spindle. *Proc. Natl. Acad. Sci.* 92:3430–3434. doi:10.1073/pnas.92.8.3430.
Gruneberg, U., R. Neef, X. Li, E.H.Y. Chan, R.B. Chalamalasetty, E.A. Nigg, and F.A. Barr. 2006. KIF14 and citron kinase act together to promote efficient cytokinesis. *J. Cell Biol.* 172:363–372. doi:10.1083/jcb.200511061.
Halet, G., and J. Carroll. 2007. Rac Activity Is Polarized and Regulates Meiotic Spindle Stability and Anchoring in Mammalian Oocytes. *Dev. Cell*. 12:309–317. doi:10.1016/j.devcel.2006.12.010.
Hara, M., Y. Abe, T. Tanaka, T. Yamamoto, E. Okumura, and T. Kishimoto. 2012. Greatwall kinase and cyclin B-Cdk1 are both critical constituents of M-phase-promoting factor. *Nat. Commun.* 3:1059. doi:10.1038/ncomms2062.
Hashimoto, N., N. Watanabe, Y. Furuta, H. Tamemoto, N. Sagata, M. Yokoyama, K. Okazaki, M. Nagayoshi, N. Takedat, Y. Ikawatll, and S. Aizawai. 1994. Parthenogenetic activation of oocytes in c-mos-deficient mice. *Nature*. 370:68—71. doi:10.1038/370068a0.
Hochegger, H., A. Klotzbücher, J. Kirk, M. Howell, K. le Guellec, K. Fletcher, T. Duncan, M. Sohail, and T. Hunt. 2001. New B-type cyclin synthesis is required between meiosis I and II during Xenopus oocyte maturation. *Development*. 128:3795–3807. doi:10.1242/dev.128.19.3795.
Holubcová, Z., M. Blayney, K. Elder, and M. Schuh. 2015. Human oocytes. Error-prone chromosome-mediated spindle assembly favors chromosome segregation defects in human oocytes. *Science*. 348:1143–1147. doi:10.1126/science.aaa9529.
Hornbeck, P.V., B. Zhang, B. Murray, J.M. Kornhauser, V. Latham, and E. Skrzypek. 2015. PhosphoSitePlus, 2014: mutations, PTMs and recalibrations. *Nucleic Acids Res.* 43:D512–D520. doi:10.1093/nar/gku1267.
Huerta-Cepas, J., D. Szklarczyk, K. Forslund, H. Cook, D. Heller, M.C. Walter, T. Rattei, D.R. Mende, S. Sunagawa, M. Kuhn, L.J. Jensen, C. von Mering, and P. Bork. 2016. eggNOG 4.5: a hierarchical orthology framework with improved functional annotations for eukaryotic, prokaryotic and viral sequences. *Nucleic Acids Res.* 44:D286–D293. doi:10.1093/nar/gkv1248.
Hughes, C.S., S. Moggridge, T. Müller, P.H. Sorensen, G.B. Morin, and J. Krijgsveld. 2019. Single-pot, solid-phase-enhanced sample preparation for proteomics experiments. *Nat. Protoc.* 14:68–85. doi:10.1038/s41596-018-0082-x.
Humphrey, S.J., S.B. Azimifar, and M. Mann. 2015. High-throughput phosphoproteomics reveals in vivo insulin signaling dynamics. *Nat. Biotechnol.* 33:990–995. doi:10.1038/nbt.3327.
Ikeda, M., S. Chiba, K. Ohashi, and K. Mizuno. 2012. Furry Protein Promotes Aurora A-mediated Polo-like Kinase 1 Activation*. *J. Biol. Chem.* 287:27670–27681.

doi:10.1074/jbc.m112.378968.
Ivanovska, I., E. Lee, K.M. Kwan, D.D. Fenger, and T.L. Orr-Weaver. 2004. The Drosophila MOS Ortholog Is Not Essential for Meiosis. *Curr. Biol.* 14:75–80. doi:10.1016/j.cub.2003.12.031.
Iwabuchi, M., K. Ohsumi, T.M. Yamamoto, W. Sawada, and T. Kishimoto. 2000. Residual Cdc2 activity remaining at meiosis I exit is essential for meiotic M–M transition in Xenopus oocyte extracts. *EMBO J.* 19:4513–4523. doi:10.1093/emboj/19.17.4513.
Jaffe, L.A., and M. Terasaki. 2004. Quantitative Microinjection of Oocytes, Eggs, and Embryos. *Methods Cell Biol.* 74:219–242. doi:10.1016/s0091-679x(04)74010-8.
Jessus, C., C. Munro, and E. Houliston. 2020. Managing the Oocyte Meiotic Arrest-Lessons from Frogs and Jellyfish. *Cells*. 9:1150. doi:10.3390/cells9051150.
Johnson, J.L., T.M. Yaron, E.M. Huntsman, A. Kerelsky, J. Song, A. Regev, T.-Y. Lin, K. Liberatore, D.M. Cizin, B.M. Cohen, N. Vasan, Y. Ma, K. Krismer, J.T. Robles, B. van de Kooij, A.E. van Vlimmeren, N. Andrée-Busch, N.F. Käufer, M.V. Dorovkov, A.G. Ryazanov, Y. Takagi, E.R. Kastenhuber, M.D. Goncalves, B.D. Hopkins, O. Elemento, D.J. Taatjes, A. Maucuer, A. Yamashita, A. Degterev, M. Uduman, J. Lu, S.D. Landry, B. Zhang, I. Cossentino, R. Linding, J. Blenis, P.V. Hornbeck, B.E. Turk, M.B. Yaffe, and L.C. Cantley. 2023. An atlas of substrate specificities for the human serine/threonine kinome. *Nature*. 613:759–766. doi:10.1038/s41586-022-05575-3.
Kudtarkar, P., and R.A. Cameron. 2017. Echinobase: an expanding resource for echinoderm genomic information. *Database J. Biol. Databases Curation*. 2017:bax074. doi:10.1093/database/bax074.
Lapasset, L., B. Pradet-Balade, V. Vergé, J. Lozano, N. Oulhen, P. Cormier, and G. Peaucellier. 2008. Cyclin B synthesis and rapamycin-sensitive regulation of protein synthesis during starfish oocyte meiotic divisions. *Mol. Reprod. Dev.* 75:1617–1626. doi:10.1002/mrd.20905.
Lefebvre, C., M.E. Terret, A. Djiane, P. Rassinier, B. Maro, and M.-H. Verlhac. 2002. Meiotic spindle stability depends on MAPK-interacting and spindle-stabilizing protein (MISS), a new MAPK substrate. *J. Cell Biol.* 157:603–613. doi:10.1083/jcb.200202052.
Liu, J., P.D. Stevens, N.E. Eshleman, and T. Gao. 2013. Protein Phosphatase PPM1G Regulates Protein Translation and Cell Growth by Dephosphorylating 4E Binding Protein 1 (4E-BP1)*. *J. Biol. Chem.* 288:23225–23233. doi:10.1074/jbc.m113.492371.
Mendez, R., and J.D. Richter. 2001. Translational control by CPEB: a means to the end. *Nat. Rev. Mol. Cell Biol.* 2:521–529. doi:10.1038/35080081.
Minshall, N., M.H. Reiter, D. Weil, and N. Standart. 2007. CPEB Interacts with an Ovary-specific eIF4E and 4E-T in Early Xenopus Oocytes*. *J. Biol. Chem.* 282:37389–37401. doi:10.1074/jbc.m704629200.
Mogessie, B., K. Scheffler, and M. Schuh. 2018. Assembly and Positioning of the Oocyte Meiotic Spindle. *Annu. Rev. Cell Dev. Biol.* 34:381–403. doi:10.1146/annurev-cellbio-100616-060553.
Mori, M., M. Hara, K. Tachibana, and T. Kishimoto. 2006. p90Rsk is required for G1 phase arrest in unfertilized starfish eggs. *Development*. 133:1823—1830. doi:10.1242/dev.02348.
Murtagh, F., and P. Legendre. 2014. Ward's Hierarchical Agglomerative Clustering Method: Which Algorithms Implement Ward's Criterion? *J. Classif.* 31:274–295. doi:10.1007/s00357-014-9161-z.
Oskarsson, M., W.L. McClements, D.G. Blair, J.V. Maizel, and G.F.V. Woude. 1980. Properties of a Normal Mouse Cell DNA Sequence (sarc) Homologous to the src Sequence of Moloney Sarcoma Virus. *Science*. 207:1222–1224. doi:10.1126/science.6243788.
Pal, D., A. Ellis, S.P. Sepúlveda-Ramírez, T. Salgado, I. Terrazas, G. Reyes, R.D.L. Rosa, J.H. Henson, and C.B. Shuster. 2020. Rac and Arp2/3-Nucleated Actin Networks Antagonize Rho During Mitotic and Meiotic Cleavages. *Front. Cell Dev. Biol.* 8:591141. doi:10.3389/fcell.2020.591141.
Perez-Riverol, Y., J. Bai, C. Bandla, D. García-Seisdedos, S. Hewapathirana, S. Kamatchinathan, D.J. Kundu, A. Prakash, A. Frericks-Zipper, M. Eisenacher, M. Walzer, S. Wang, A. Brazma, and

J.A. Vizcaíno. 2022. The PRIDE database resources in 2022: a hub for mass spectrometry-based proteomics evidences. *Nucleic Acids Res.* 50:D543–D552. doi:10.1093/nar/gkab1038.
Phillips, K.P., M.A.F. Petrunewich, J.L. Collins, R.A. Booth, X.J. Liu, and J.M. Baltz. 2002. Inhibition of MEK or cdc2 Kinase Parthenogenetically Activates Mouse Eggs and Yields the Same Phenotypes as Mos−/− Parthenogenotes. *Dev. Biol.* 247:210–223. doi:10.1006/dbio.2002.0680.
Sagata, N., M. Oskarsson, T. Copeland, J. Brumbaugh, and G.F.V. Woude. 1988. Function of c-mos proto-oncogene product in meiotic maturation in Xenopus oocytes. *Nature*. 335:519–525. doi:10.1038/335519a0.
Samwer, M., H. Dehne, F. Spira, M. Kollmar, D.W. Gerlich, H. Urlaub, and D. Görlich. 2013. The nuclear F-actin interactome of Xenopus oocytes reveals an actin-bundling kinesin that is essential for meiotic cytokinesis. *EMBO J.* 32:1886–1902. doi:10.1038/emboj.2013.108.
Schindelin, J., I. Arganda-Carreras, E. Frise, V. Kaynig, M. Longair, T. Pietzsch, S. Preibisch, C. Rueden, S. Saalfeld, B. Schmid, J.-Y. Tinevez, D.J. White, V. Hartenstein, K. Eliceiri, P. Tomancak, and A. Cardona. 2012. Fiji: an open-source platform for biological-image analysis. *Nat. Methods*. 9:676–682. doi:10.1038/nmeth.2019.
Schuh, M., and J. Ellenberg. 2007. Self-organization of MTOCs replaces centrosome function during acentrosomal spindle assembly in live mouse oocytes. *Cell*. 130:484–498. doi:10.1016/j.cell.2007.06.025.
Sensui, N., M. Yoshida, and K. Tachibana. 2012. Role of Mos/MEK/ERK cascade and Cdk1 in Ca2+ oscillations in fertilized ascidian eggs. *Dev. Biol.* 367:208–215. doi:10.1016/j.ydbio.2012.05.011.
Severson, A.F., G. von Dassow, and B. Bowerman. 2016. Chapter Five Oocyte Meiotic Spindle Assembly and Function. *Curr. Top. Dev. Biol.* 116:65–98. doi:10.1016/bs.ctdb.2015.11.031.
Shakya, A., S. Park, N. Rana, and J.T. King. 2020. Liquid-Liquid Phase Separation of Histone Proteins in Cells: Role in Chromatin Organization. *Biophys. J.* 118:753–764. doi:10.1016/j.bpj.2019.12.022.
Sheets, M.D., M. Wu, and M. Wickens. 1995. Polyadenylation of c-mos mRNA as a control point in Xenopus meiotic maturation. *Nature*. 374:511–516. doi:10.1038/374511a0.
Slep, K.C., and R.D. Vale. 2007. Structural Basis of Microtubule Plus End Tracking by XMAP215, CLIP-170, and EB1. *Mol. Cell*. 27:976–991. doi:10.1016/j.molcel.2007.07.023.
Sluder, G., F.J. Miller, and K. Lewis. 1993. Centrosome Inheritance in Starfish Zygotes II: Selective Suppression of the Maternal Centrosome during Meiosis. *Dev. Biol.* 155:58–67. doi:10.1006/dbio.1993.1006.
Strickland, L., G. von Dassow, J. Ellenberg, V. Foe, P. Lenart, and D. Burgess. 2004. Light Microscopy of Echinoderm Embryos. *Methods Cell Biol.* 74:371–409. doi:10.1016/s0091-679x(04)74016-9.
Swartz, S.Z., H.T. Nguyen, B.C. McEwan, M.E. Adamo, I.M. Cheeseman, and A.N. Kettenbach. 2021. Selective dephosphorylation by PP2A-B55 directs the meiosis I - meiosis II transition in oocytes. *eLife*. 10:e70588. doi:10.7554/elife.70588.
Tachibana, K., D. Tanaka, T. Isobe, and T. Kishimoto. 2000. c-Mos forces the mitotic cell cycle to undergo meiosis II to produce haploid gametes. *Proc. Natl. Acad. Sci.* 97:14301—14306. doi:10.1073/pnas.97.26.14301.
Terret, M.E., C. Lefebvre, A. Djiane, P. Rassinier, J. Moreau, B. Maro, and M.-H. Verlhac. 2003. DOC1R: a MAP kinase substrate that control microtubule organization of metaphase II mouse oocytes. *Development*. 130:5169–5177. doi:10.1242/dev.00731.
Ucar, H., K. Tachibana, and T. Kishimoto. 2013. The Mos–MAPK pathway regulates Diaphanous-related formin activity to drive cleavage furrow closure during polar body extrusion in starfish oocytes. *J Cell Sci*. 126:5153—5165. doi:10.1242/jcs.130476.
Valdez, V.A., L. Neahring, S. Petry, and S. Dumont. 2023. Mechanisms underlying spindle assembly and robustness. *Nat. Rev. Mol. Cell Biol.* 1–20. doi:10.1038/s41580-023-00584-0.

Veld, P.J.H. in 't, S. Wohlgemuth, C. Koerner, F. Müller, P. Janning, and A. Musacchio. 2021. Reconstitution and use of highly active human CDK1:Cyclin-B:CKS1 complexes. *Protein Sci.* doi:10.1002/pro.4233.

Verlhac, M.H., J.Z. Kubiak, M. Weber, G. Geraud, W.H. Colledge, M.J. Evans, and B. Maro. 1996. Mos is required for MAP kinase activation and is involved in microtubule organization during meiotic maturation in the mouse. *Development*. 122:815–822. doi:10.1242/dev.122.3.815.

Verlhac, M.-H., C. Lefebvre, P. Guillaud, P. Rassinier, and B. Maro. 2000. Asymmetric division in mouse oocytes: with or without Mos. *Curr. Biol.* 10:1303–1306. doi:10.1016/s0960-9822(00)00753-3.

Wesolowska, N., I. Avilov, P. Machado, C. Geiss, H. Kondo, M. Mori, and P. Lenart. 2020. Actin assembly ruptures the nuclear envelope by prying the lamina away from nuclear pores and nuclear membranes in starfish oocytes. *eLife*. 9:e49774. doi:10.7554/elife.49774.

Wessel, G.M., A.M. Reich, and P.C. Klatsky. 2010. Use of Sea Stars to Study Basic Reproductive Processes. *Syst. Biol. Reprod. Med.* 56:236–245. doi:10.3109/19396361003674879.

Wu, J.Q., and S. Kornbluth. 2008. Across the meiotic divide - CSF activity in the post-Emi2/XErp1 era. *J. Cell Sci.* 121:3509–3514. doi:10.1242/jcs.036855.

Figure 1

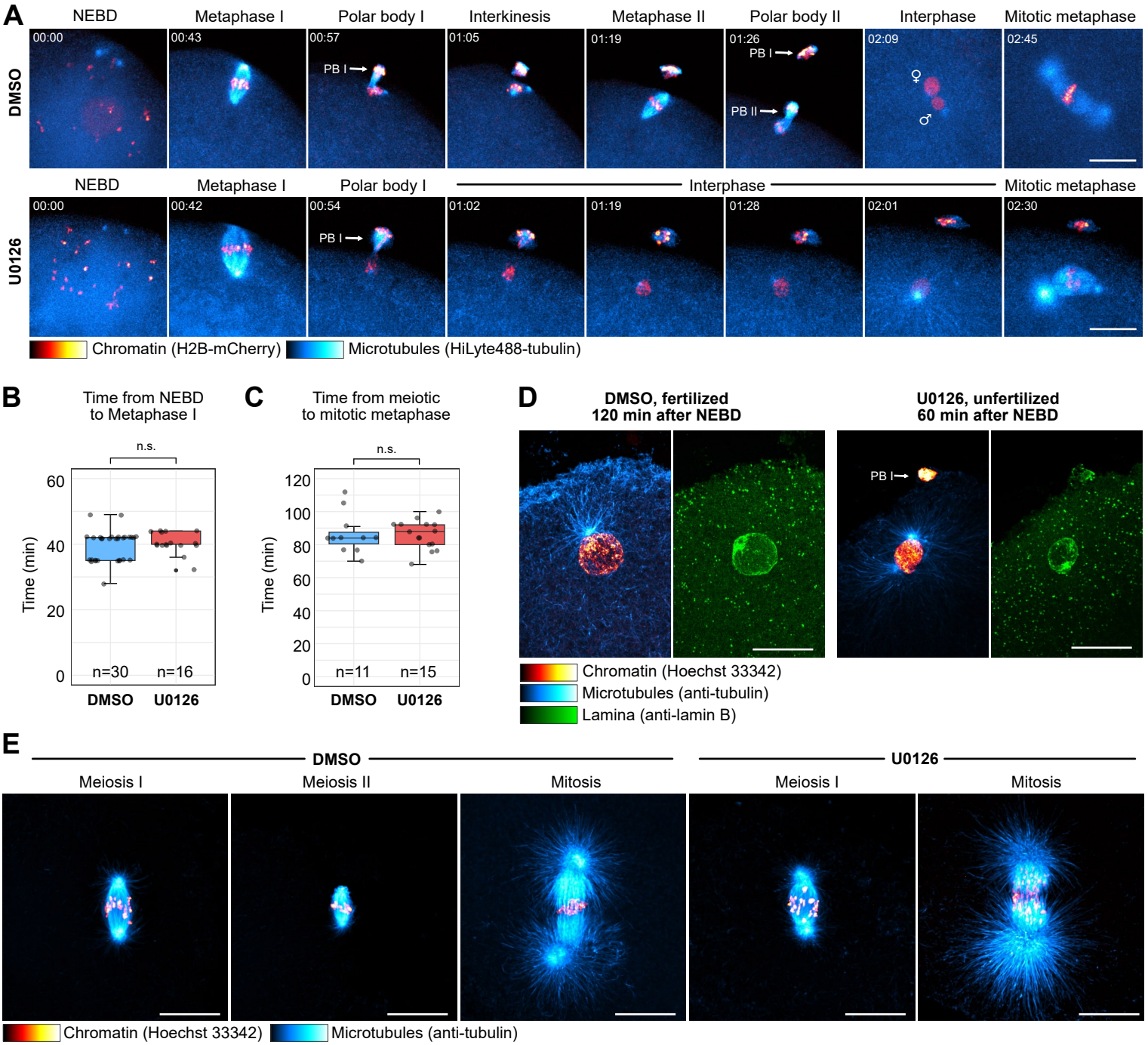
A
NEBD
Metaphase I
Polar body I
Interkinesis
Metaphase II
Polar body II
Interphase
Mitotic metaphase
DMSO
00:00
00:43
00:57
PB I
01:05
01:19
01:26
PB I
PB II
02:09
♀
♂
02:45
U0126
00:00
00:42
00:54
PB I
01:02
01:19
01:28
02:01
02:30
Chromatin (H2B-mCherry)
Microtubules (HiLyte488-tubulin)
B
Time from NEBD to Metaphase I
n.s.
Time (min)
n=30
n=16
DMSO
U0126
C
Time from meiotic to mitotic metaphase
n.s.
Time (min)
n=11
n=15
DMSO
U0126
D
DMSO, fertilized 120 min after NEBD
U0126, unfertilized 60 min after NEBD
PB I
Chromatin (Hoechst 33342)
Microtubules (anti-tubulin)
Lamina (anti-lamin B)
E
DMSO
U0126
Meiosis I
Meiosis II
Mitosis
Meiosis I
Mitosis
Chromatin (Hoechst 33342)
Microtubules (anti-tubulin)
F
Half-spindle length
Centro-somal area
Spindle width
G
Half-spindle length
Half-spindle length (µm)
n=30
n=30
n=22
n=20
n=28
Meio I
Meio II
Mito
Meio I
Mito
DMSO
U0126
Spindle width
Spindle width (µm)
n=49
n=39
n=11
n=9
n=9
Meio I
Meio II
Mito
Meio I
Mito
DMSO
U0126
Diameter of centrosomal area
Centrosomal area (µm)
n=30
n=30
n=22
n=20
n=28
Meio I
Meio II
Mito
Meio I
Mito
DMSO
U0126

Figure 2

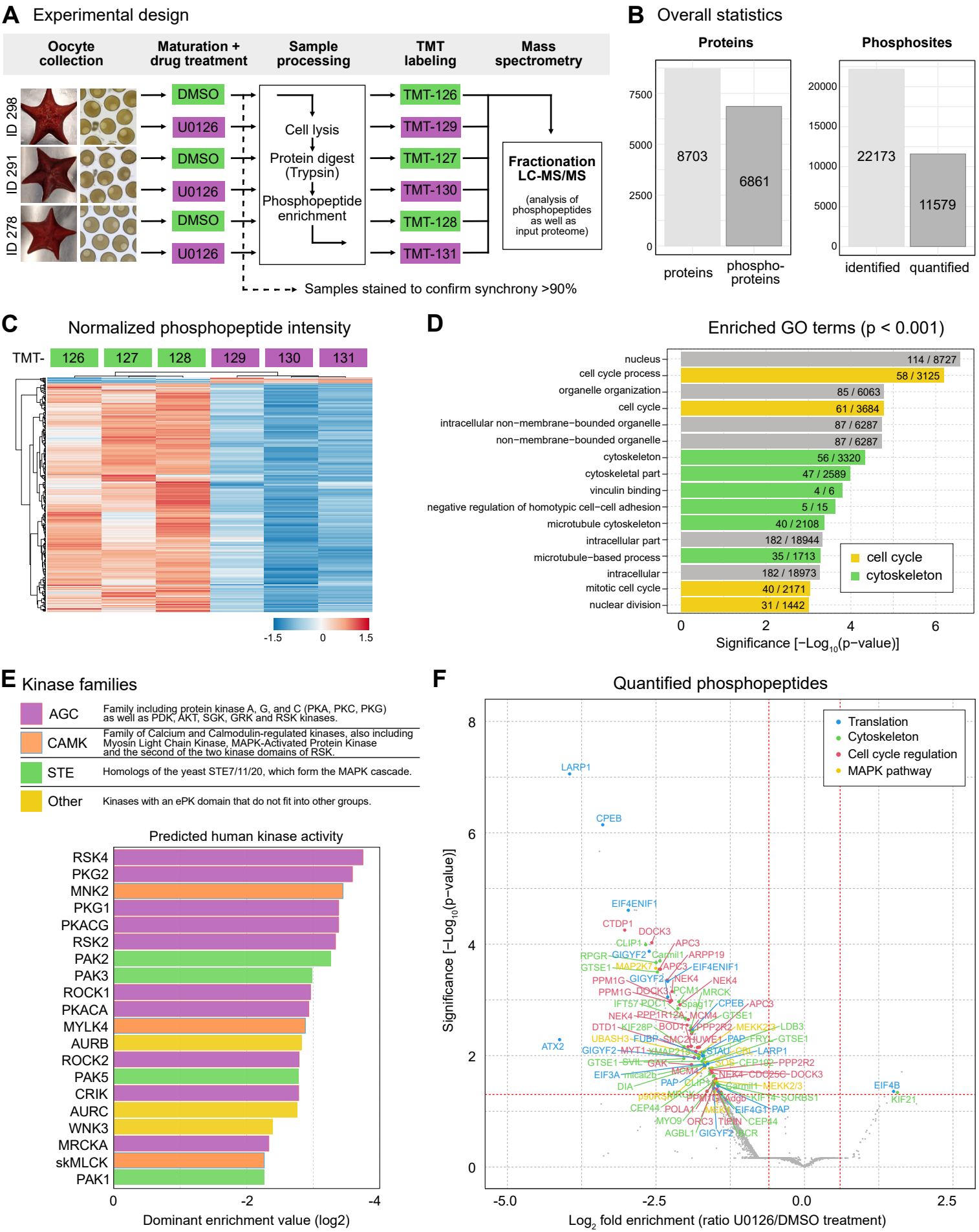
A Experimental design
Oocyte collection
Maturation + drug treatment
Sample processing
TMT labeling
Mass spectrometry
ID 298
ID 291
ID 278
DMSO
U0126
DMSO
U0126
DMSO
U0126
Cell lysis
Protein digest (Trypsin)
Phosphopeptide enrichment
TMT-126
TMT-129
TMT-127
TMT-130
TMT-128
TMT-131
Fractionation LC-MS/MS
(analysis of phosphopeptides as well as input proteome)
Samples stained to confirm synchrony >90%
B Overall statistics
Proteins
Phosphosites
8703
6861
22173
11579
proteins
phospho-proteins
identified
quantified
C Normalized phosphopeptide intensity
TMT- 126 127 128 129 130 131
-1.5 0 1.5
D Enriched GO terms (p < 0.001)
nucleus 114 / 8727
cell cycle process 58 / 3125
organelle organization 85 / 6063
cell cycle 61 / 3684
intracellular non−membrane−bounded organelle 87 / 6287
non−membrane−bounded organelle 87 / 6287
cytoskeleton 56 / 3320
cytoskeletal part 47 / 2589
vinculin binding 4 / 6
negative regulation of homotypic cell−cell adhesion 5 / 15
microtubule cytoskeleton 40 / 2108
intracellular part 182 / 18944
microtubule−based process 35 / 1713
intracellular 182 / 18973
mitotic cell cycle 40 / 2171
nuclear division 31 / 1442
cell cycle
cytoskeleton
Significance [−Log10(p−value)]
E Kinase families
AGC Family including protein kinase A, G, and C (PKA, PKC, PKG) as well as PDK, AKT, SGK, GRK and RSK kinases.
CAMK Family of Calcium and Calmodulin-regulated kinases, also including Myosin Light Chain Kinase, MAPK-Activated Protein Kinase and the second of the two kinase domains of RSK.
STE Homologs of the yeast STE7/11/20, which form the MAPK cascade.
Other Kinases with an ePK domain that do not fit into other groups.
Predicted human kinase activity
RSK4
PKG2
MNK2
PKG1
PKACG
RSK2
PAK2
PAK3
ROCK1
PKACA
MYLK4
AURB
ROCK2
PAK5
CRIK
AURC
WNK3
MRCKA
skMLCK
PAK1
Dominant enrichment value (log2)
F Quantified phosphopeptides
Translation
Cytoskeleton
Cell cycle regulation
MAPK pathway
LARP1
CPEB
EIF4ENIF1
CTDP1
DOCK3
ATX2
EIF4B
KIF21
Significance [−Log10(p−value)]
Log2 fold enrichment (ratio U0126/DMSO treatment)

Figure 3

A

	Name	KEGG	Protein IDs	Peptide	MS scan IDs	p-adj	Enrichment
MAPK module	MEK1	K04369	XP_038079443.1, PMI_017007	NLTLPVKPDDSAPSNAVNNSS*ASMAAIAK	51401	0.0444	-1.5136
	p90RSK	K04373	XP_038049299.1, PMI_022459	T*PKDSPGLPPSASAHQLFR	44589	0.0165	-1.6801
cdk1-Cyclin B module	PPP2R2	K04354	XP_038070796.1, PMI_020469	KRPLSTSDGT*AK	22877	0.0180	-1.5714
	PPP2R2	K04354	XP_038070796.1, PMI_020469	RPLS*TSDGTAKK	23882	0.0040	-1.8997
	MYT1	K06633	PMI_008112	AVSFRQSEPSVLQS*PHYNEK	41151	0.0109	-1.8548
	APC3	K03350	PMI_002534, XP_038047876.1, PMI_014580	LFS*NNSVKENATK	45583	0.0003	-2.4236
	APC3	K03350	PMI_002534, XP_038047876.1, PMI_014580	LFS*NNS*VK	49005, 45078	0.0003	-2.4422
	CDC25C	K05866	XP_038070722.1	NRS*ETIMWEACNDKENVDIQNK	42276	0.0262	-1.4918
	ARPP19		XP_038072705.1, PMI_013584	KQS*TEISK	23112	0.0004	-2.3112
Translational activation module	LARP1	K18757	PMI_014589	EGRES*VDSPR	8801, 7715	0.0000	-3.9525
	CPEB	K02602	XP_038045408.1, PMI_005839, PMI_001490	HTS*NNPGRPEK	10213	0.0000	-3.3840
	CPEB	K02602	XP_038045408.1, PMI_005839, PMI_001490	YPS*QEIQQDYEK	37277	0.0035	-1.8924
	EIF4ENIF1	K18728	PMI_009884	KS*EPDGESGEKEEEGGDK	21052, 19560	0.0000	-2.9642
	EIF3A	K03254	PMI_009181	S*AGIKDEEDEPR	22666	0.0140	-1.6728
	EIF4B	K03258	XP_038044282.1	SNEDDSAFHKEEPLSPTSPTAPKS*PK	36461	0.0440	1.5003
	EIF4G1	K03260	XP_038075416.1	VIQRVS*QTIK	36609	0.0444	-1.4466
	PAP	K14376	XP_038074837.1, PMI_002048	LPS*GELPDMSSPMPK	53218, 49713, 47545	0.0111	-1.7180
	PPM1G	K17499	PMI_005456, PMI_016115	KAS*ESTPTDDDDSKR	16212, 19904, 17237	0.0011	-2.2632
	ATX2	K23625	PMI_011421, XP_038075475.1, PMI_025445	DGTRGHS*PQHASVQR	6500	0.0165	-4.1221
Microtubule module	CLIP1	K10421	XP_038055294.1, PMI_010288	KTS*TSTVNSETSQR	14508	0.0001	-2.6735
	CLIP1	K10421	XP_038055294.1, PMI_010288	S*VDLTGNKPSLTNK	42275	0.0232	-1.5252
	XMAP215	K16803	XP_038047612.1, PMI_009212	SNRLS*QGSMSSEPVNGSAEQER	22932	0.0107	-1.7741
	GTSE1	K10129	XP_038054192.1	KES*DESQGSDSQESK	15744	0.0003	-2.4737
	GTSE1	K10129	XP_038054192.1	LPSTPST*PVHQDKK	33139, 34006	0.0038	-1.8905
	GTSE1	K10129	XP_038054192.1	LLSSDQS*ATKPVGR	38688	0.0113	-2.0316
	POC1	K16482	XP_038054221.1, PMI_022968, PMI_011690	S*TGADINAHSEPK	21180	0.0022	-2.0017
	PCM1	K16537	XP_038056285.1, XP_038056290.1	LLS*VQQQLR	46891	0.0011	-2.1149
	CEP44	K16761	XP_038055484.1	HAS*GSLVR	15956	0.0211	-1.5896
	CEP44	K16761	XP_038055484.1	RVS*VSVNELR	34019	0.0482	-1.3946
	CEP192	K16725	XP_038068323.1	RPS*FGTGHIKT*PEGR	27259	0.0172	-1.5904
	KIF21	K10395	XP_038053367.1, XP_038053368.1	LHSHSDRENES*ADEKEDAAEK	18719	0.0460	1.5649
	KIF14	K17915	PMI_006555, XP_038045418.1	IDS*PMT*PLKR	40449	0.0344	-1.4586
	FRYL		XP_038055332.1, PMI_004592, PMI_010187	RS*S*SGGTLEK	17295	0.0113	-1.6849
Cortical contraction module	MYPT1	K06270	XP_038073240.1, XP_038073245.1	TGS*ASTDTSSTSVR	12906	0.0023	-1.9539
	MRCK	K16307	XP_038071518.1	RGGGS*VGAENNEVK	17206	0.0032	-1.9099
	MRCK	K16307	XP_038071518.1	RLES*EKNTLSHR	21479	0.0278	-1.5109
	mDia2	K16688	XP_038063096.1, PMI_026018, PMI_028305	LQSRPS*VEEEEAHQEYER	26257	0.0146	-1.6930
	MYO9	K10360	XP_038073351.1, PMI_008384	KQS*DPQQAAEALGLPSDKPGK	42738	0.0337	-1.5479
	BCR	K08878	XP_038059104.1	LS*TPDVEILNVR	53153	0.0480	-1.4272

B

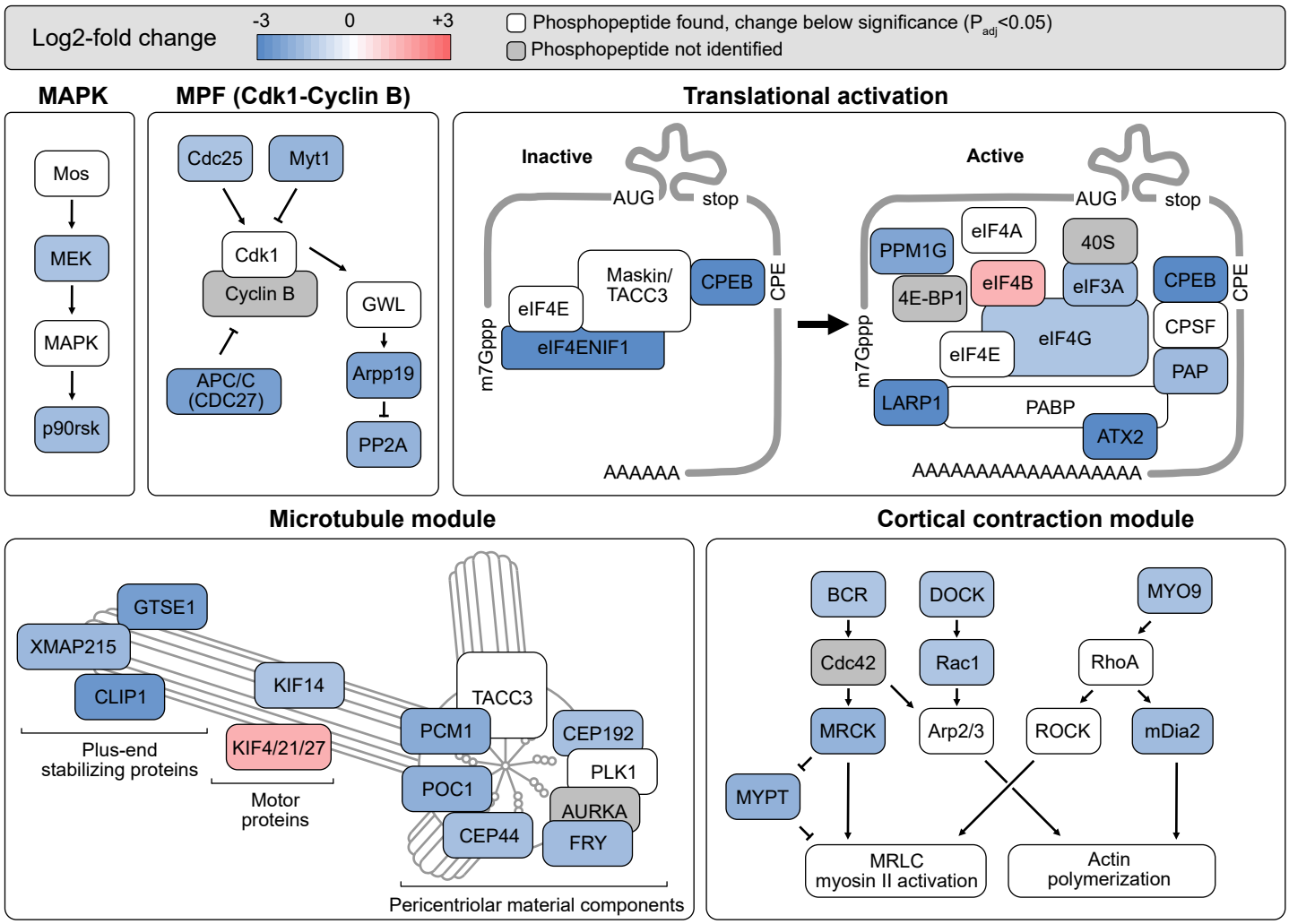

Figure 4.

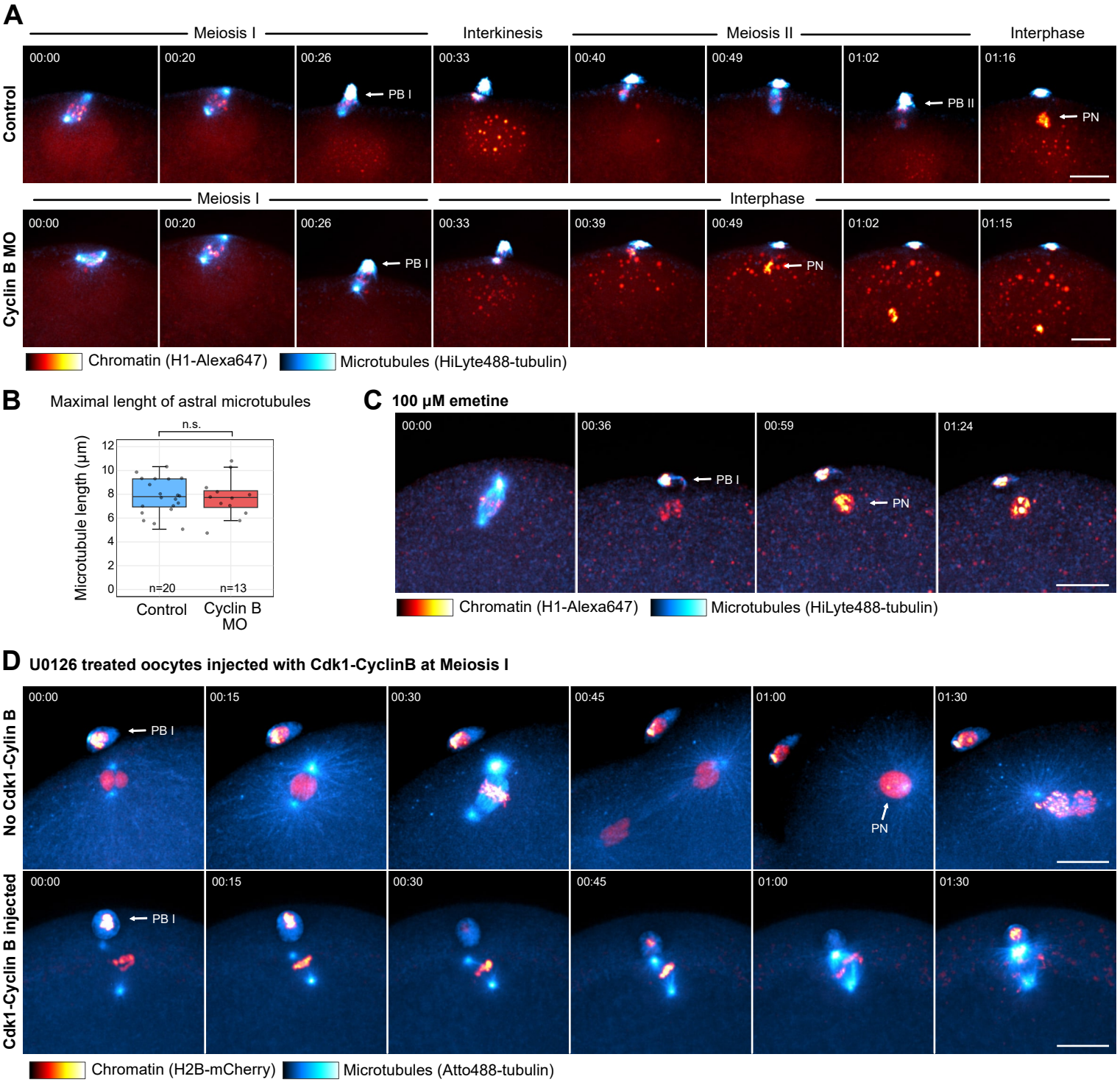
A
Meiosis I
Interkinesis
Meiosis II
Interphase
Control
00:00
00:20
00:26
PB I
00:33
00:40
00:49
01:02
PB II
01:16
PN
Meiosis I
Interphase
Cyclin B MO
00:00
00:20
00:26
PB I
00:33
00:39
00:49
PN
01:02
01:15
Chromatin (H1-Alexa647)
Microtubules (HiLyte488-tubulin)
B
Maximal lenght of astral microtubules
n.s.
Microtubule length (µm)
12
10
8
6
4
2
0
n=20
n=13
Control
Cyclin B MO
C
100 µM emetine
00:00
00:36
PB I
00:59
PN
01:24
Chromatin (H1-Alexa647)
Microtubules (HiLyte488-tubulin)
D
U0126 treated oocytes injected with Cdk1-CyclinB at Meiosis I
No Cdk1-Cylin B
00:00
PB I
00:15
00:30
00:45
01:00
PN
01:30
Cdk1-Cyclin B injected
00:00
PB I
00:15
00:30
00:45
01:00
01:30
Chromatin (H2B-mCherry)
Microtubules (Atto488-tubulin)

Figure 5

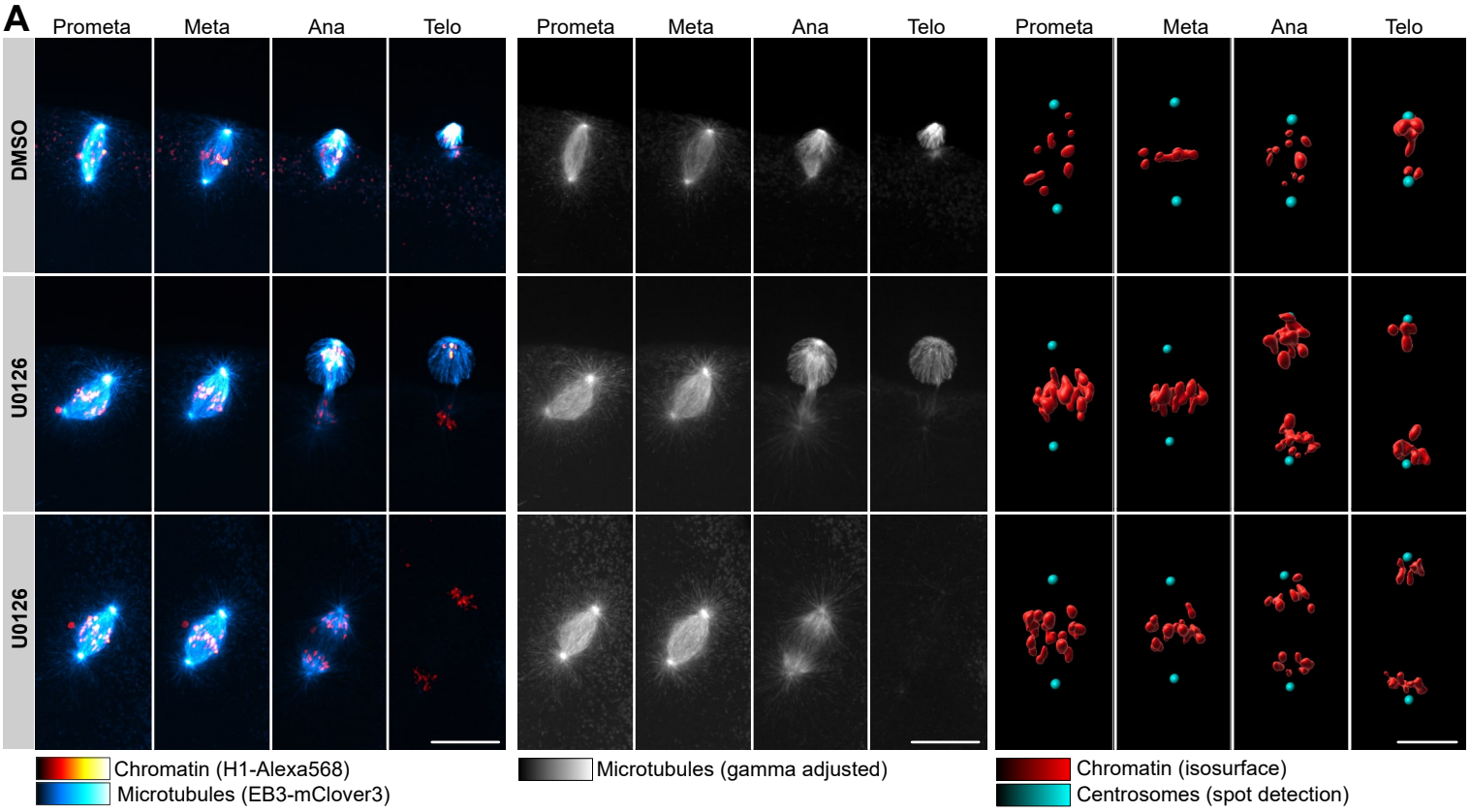
A
Prometa
Meta
Ana
Telo
DMSO
U0126
U0126
Chromatin (H1-Alexa568)
Microtubules (EB3-mClover3)
Microtubules (gamma adjusted)
Chromatin (isosurface)
Centrosomes (spot detection)

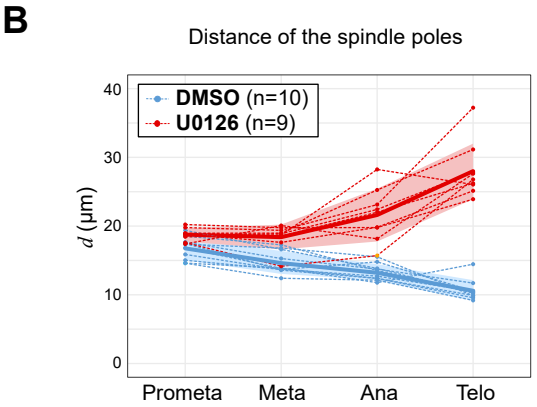
B
Distance of the spindle poles
DMSO (n=10)
U0126 (n=9)
d (µm)
0
10
20
30
40
Prometa
Meta
Ana
Telo

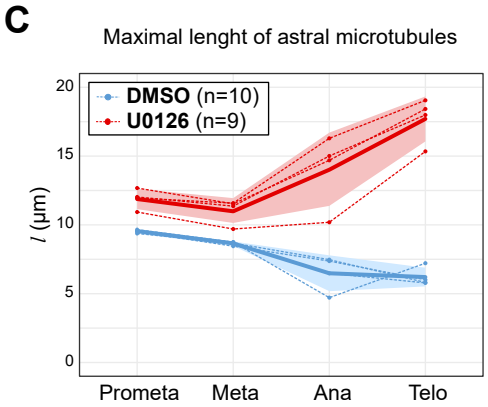
C
Maximal lenght of astral microtubules
DMSO (n=10)
U0126 (n=9)
l (µm)
0
5
10
15
20
Prometa
Meta
Ana
Telo

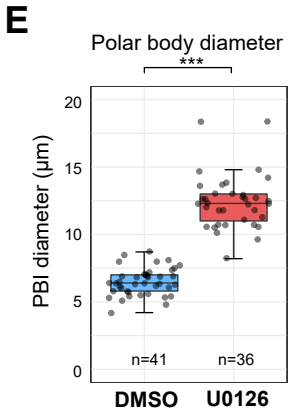
E
Polar body diameter
***
PBI diameter (µm)
0
5
10
15
20
n=41
n=36
DMSO
U0126

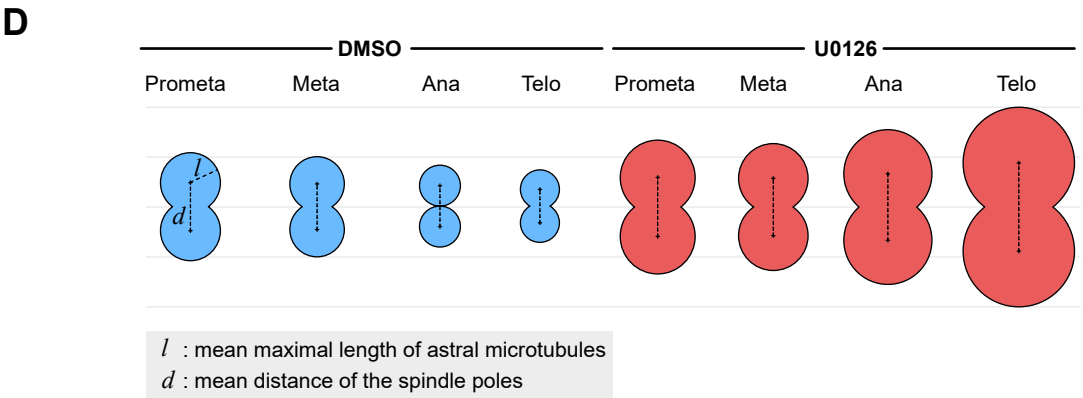
D
DMSO
U0126
Prometa
Meta
Ana
Telo
Prometa
Meta
Ana
Telo
l
d
l : mean maximal length of astral microtubules
d : mean distance of the spindle poles

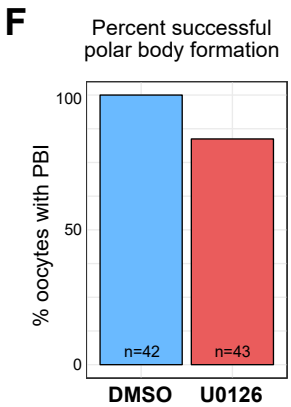
F
Percent successful polar body formation
% oocytes with PBI
0
50
100
n=42
n=43
DMSO
U0126

Figure 6

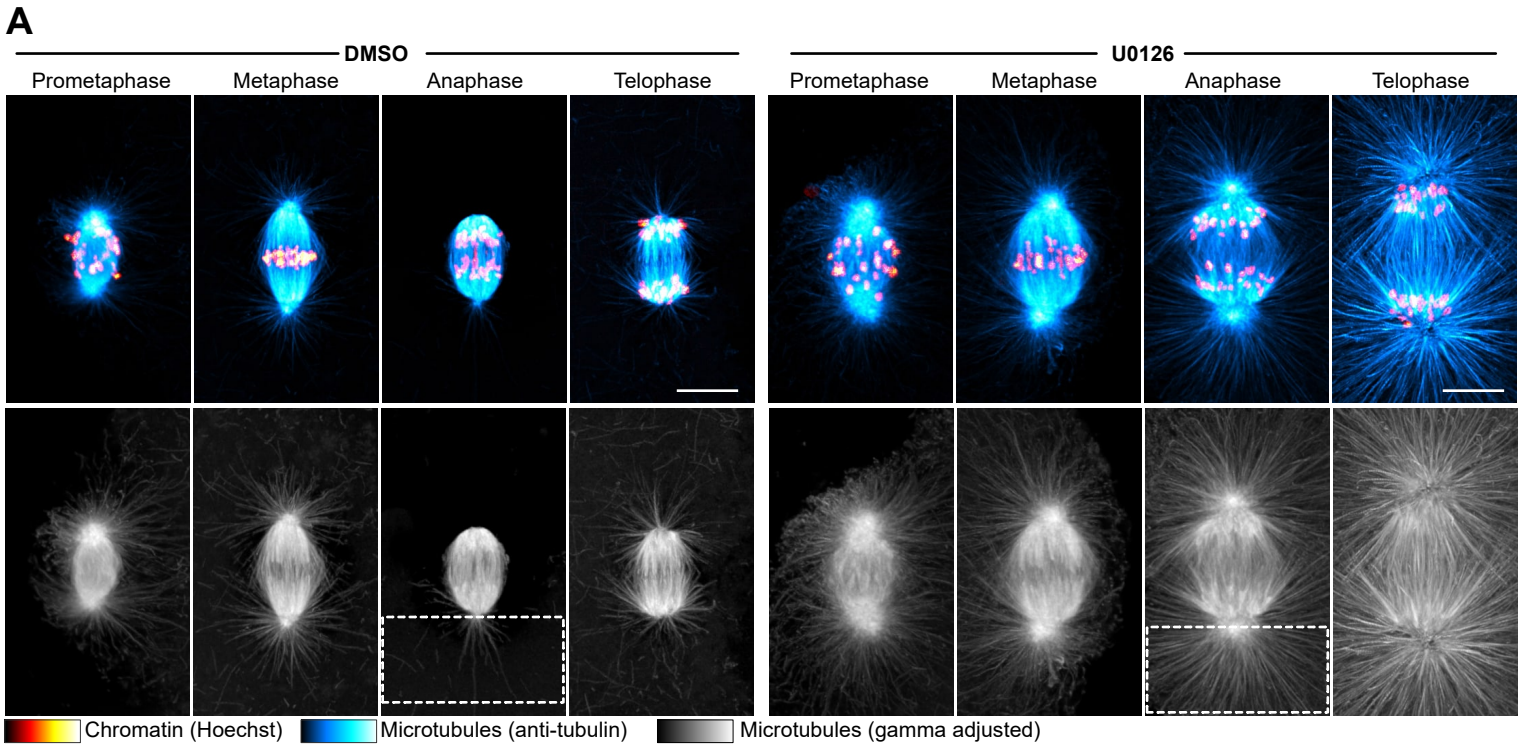
A
DMSO
U0126
Prometaphase
Metaphase
Anaphase
Telophase
Prometaphase
Metaphase
Anaphase
Telophase
Chromatin (Hoechst)
Microtubules (anti-tubulin)
Microtubules (gamma adjusted)

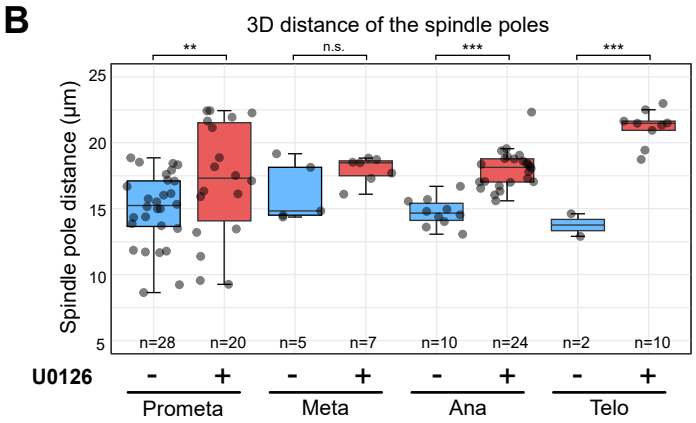
B
3D distance of the spindle poles
Spindle pole distance (µm)
25
20
15
10
5
**
n.s.
***
***
n=28
n=20
n=5
n=7
n=10
n=24
n=2
n=10
U0126
-
+
-
+
-
+
-
+
Prometa
Meta
Ana
Telo

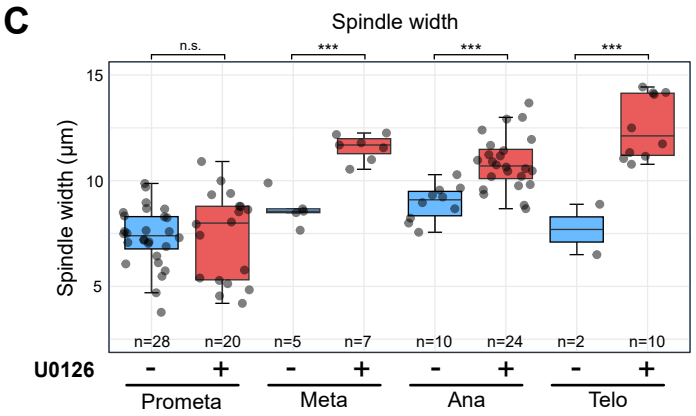
C
Spindle width
Spindle width (µm)
15
10
5
n.s.
***
***
***
n=28
n=20
n=5
n=7
n=10
n=24
n=2
n=10
U0126
-
+
-
+
-
+
-
+
Prometa
Meta
Ana
Telo

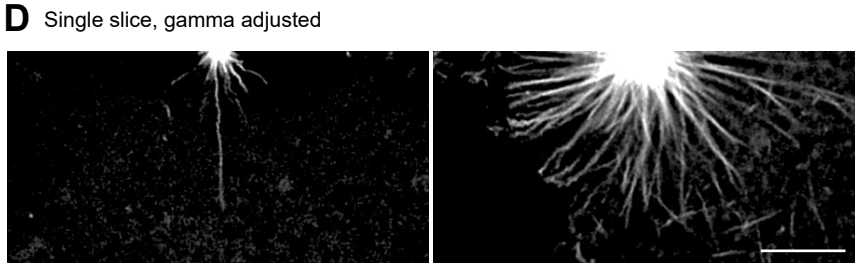
D
Single slice, gamma adjusted

Figure 7

A Mos-MAPK facilitates Cyclin B translation to drive meiosis II

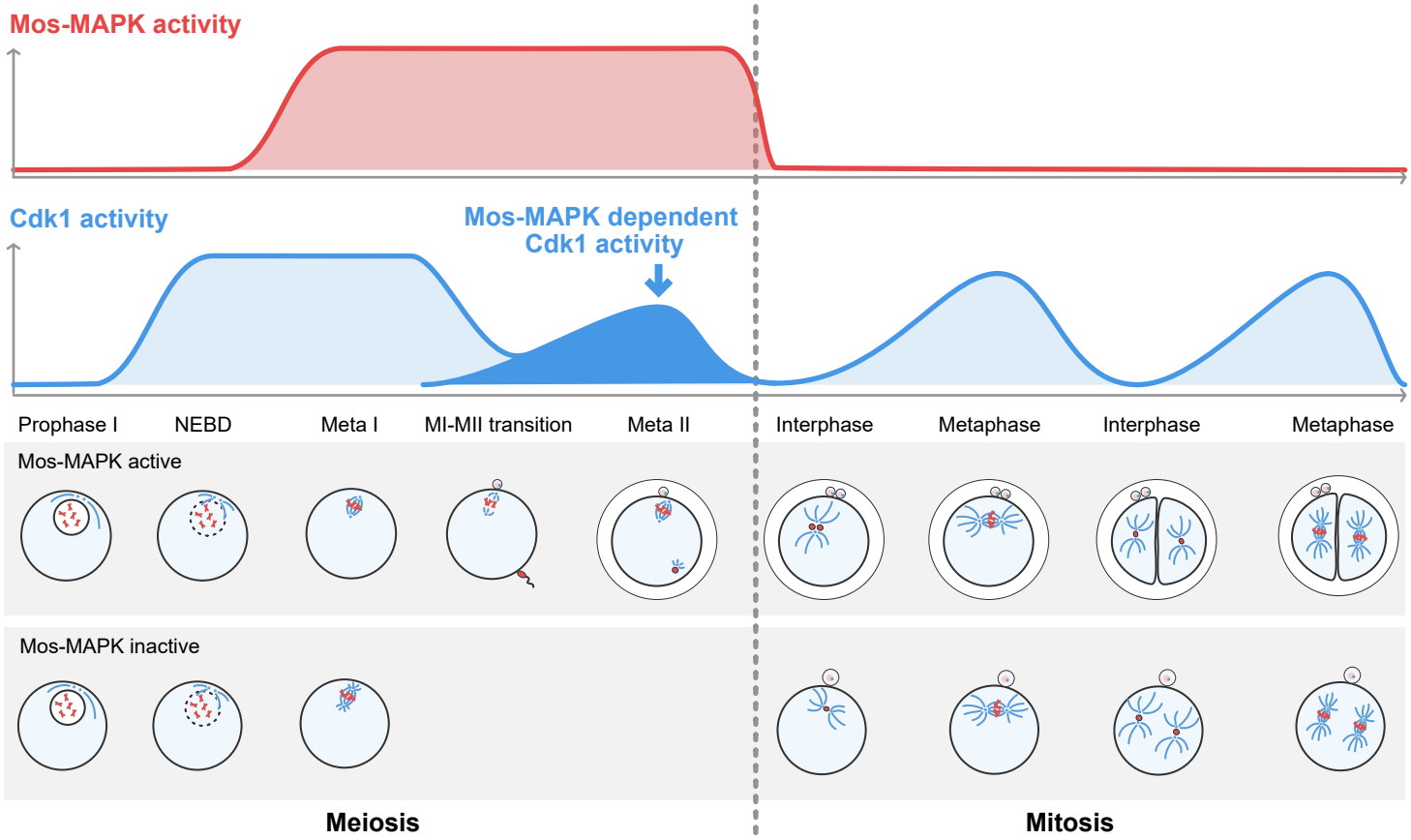
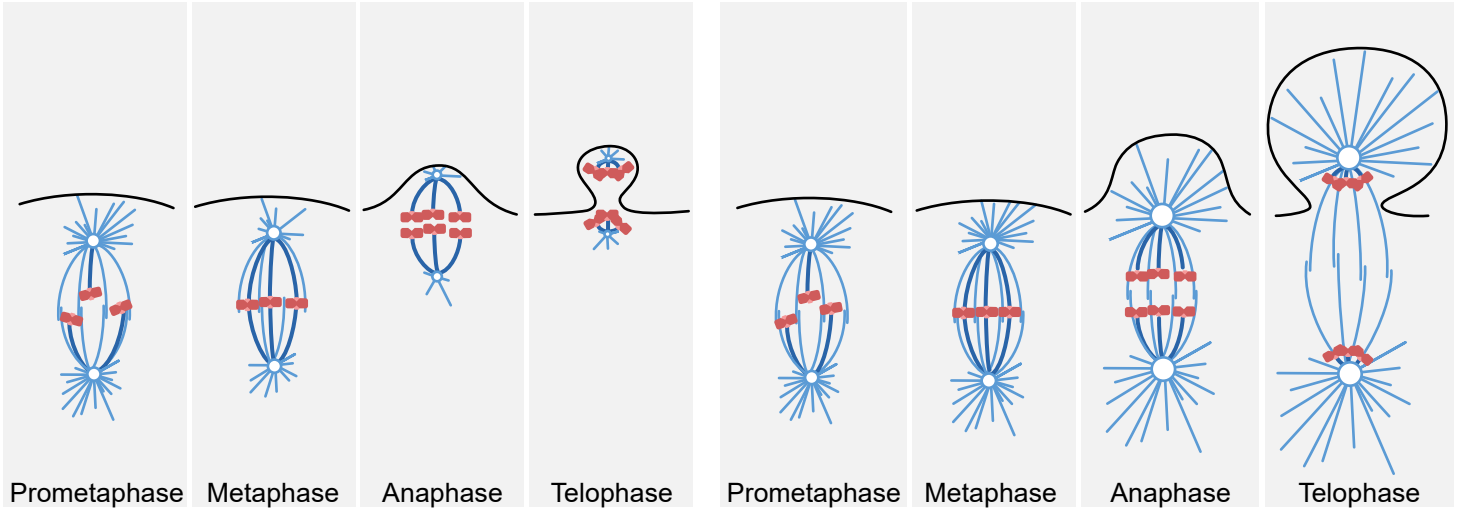
B Mos-MAPK downregulates centrosomal microtubule nucleation and prevents anaphase B